UNIVERSITY OF OKLAHOMA
GRADUATE COLLEGE

SPATIOTEMPORAL TRENDS AND ENVIRONMENTAL CONTROLS OF TURBULENCE NEAR THUNDERSTORMS OVER THE UNITED STATES

A THESIS
SUBMITTED TO THE GRADUATE FACULTY
in partial fulfillment of the requirements for the
Degree of
MASTER OF SCIENCE

by COLE HARTMAN
Norman, Oklahoma
2026

Downloaded from SHAREOK. Persistent Handle URL: https://hdl.handle.net/11244/342840

SPATIOTEMPORAL TRENDS AND ENVIRONMENTAL CONTROLS OF TURBULENCE NEAR THUNDERSTORMS OVER THE UNITED STATES

A THESIS APPROVED FOR THE
SCHOOL OF METEOROLOGY

BY THE COMMITTEE CONSISTING OF

Dr. Stacey Hitchcock (Chair)

Dr. Jason Furtado

Dr. Cameron Homeyer

©Copyright by COLE HARTMAN 2026

All Rights Reserved.

Acknowledgments

First I want to thank Dr. Stacey Hitchcock for being an excellent advisor throughout this project. I also extend great thanks to my committee members Dr. Jason Furtado and Dr. Cameron Homeyer for their help with this project. I would like to thank Dr. Todd Lane for his contributions and support throughout my master's work. I would like to thank the NCAR Research Application Laboratory's (RAL) turbulence group for their effort to support this work. In particular, we thank Wiebke Deierling for her continued assistance with this work and Greg Meymaris for his work with the EDR data acquisition and advice on best-use practices. I give thanks to JD Heaton for his work done with the datasets done during the 2025 REU program at the University of Oklahoma. I would also like to thank the airline companies that contribute to the archive of commercial EDR data. In addition, I want to thank Shawn Riley and Corey Coffey for their work maintaining the computational resources used for this project. Lastly, thanks to all of my family and friends for their support during my time as a master's student.

Table of Contents

Acknowledgments iv

List of Figures vii

Abstract ix

1 Literature Review of Turbulence 1
1.1 Introduction 1
1.2 Motivation 2
1.3 History 3
1.4 Types 6
1.5 Mechanisms 9
1.6 Detection 13
1.7 Nowcasting/Forecasting 15
1.8 Research Objectives 17

2 A Climatology Of Turbulence Near Thunderstorms Over The United States 20
2.1 Introduction 20
2.2 Data and Methods 23
2.2.1 Data Sources 23
2.2.2 Climatological Metrics 26
2.3 Results 28
2.3.1 Turbulence as a Function of Distance From Storms 28
2.3.2 Spatial Patterns of Convection and Near Storm Turbulence Over the U.S. 29
2.3.3 Seasonal Breakdown 32
2.3.4 Convective Influence on Turbulence Risk 35
2.3.5 Environmental Modulation of Turbulence Near Thunderstorms . 38
2.3.6 Temporal Patterns in Turbulence Near Convection 42
2.4 Discussion 44
2.4.1 Key Findings and Physical Interpretation 44
2.4.2 Comparison with Prior Studies 47
2.4.3 Methodological Limitations 49

2.4.4 Conclusions 50

3 Synthesis and Future Work 53
3.1 Synthesis of Findings 53
3.2 Broader Context 55
3.3 Future Work 56

Reference List 58

List of Figures

2.1 Number of EDR observations in each 0.5° x 0.5° bin from 2009-2014. . 24

2.2 Relative risk (RR) as a function of a) vertical distance from echo top where negative distances denote within storm boundaries and b) horizontal distance from 10 dBZ boundary. Blue shading represents the 95% confidence intervals, and a dashed line is placed at RR=2. 28

2.3 Convective percentage as a function of EDR threshold. Each threshold includes all observations in the dataset greater than that EDR threshold. 29

2.4 Spatial distribution of a) total storm objects over a 0.02° x 0.02° grid, b) convective percentage (%), and c) return interval of all MoG turbulence (hours) across the United States from 2009-2014 on a 1° x 1° grid. A Gaussian smoothing filter (sigma=5 for convective frequency, sigma=1 for other plots) has been applied to each plot. 31

2.5 Bootstrapped relative risk as a function of a) vertical distance from echo top and b) horizontal distance from 10 dBz echo, where negative values are within storm boundaries. Results are stratified by climatological seasons (winter=DJF, spring=MAM, summer=JJA, fall = SON). Shading represents the 90% confidence intervals at each level. Dashed lines are marked at relative risk equal to 2. 33

2.6 Seasonal spatial patterns of convective frequency (top row), convective percentage (middle row), and return interval of MoG turbulence (hours; bottom row). A Gaussian smoothing filter (sigma=5 for convective frequency, sigma=1 for other plots) has been applied to each plot. 33

2.7 (a) Relative risk of MoG turbulence vs wind speed stratified by convective (<70 km from 10 dBZ boundary) and non-convective (>70 km from 10 dBZ boundary) and (b) percent difference between convective and non-convective environments. Shaded areas represent the 95% confidence intervals after bootstrapping. 36

2.8 The same as Fig. 2.7a, but stratified by season. Due to limited sampling of wintertime convection in weak wind environments, winter data are only presented for wind speeds exceeding 20 m/s. 37

2.9 2D histogram of (a) wind speed (m/s) vs altitude (km) filled with conditional risk in LT70km environments, (b) same as (a) but in GT70km environments, (c) the same as (a) but filled with percent difference between convective and non-convective environments, (d)-(f) the same as (a)-(c) but for stability (K/km), and (g)-(i) the same as (a)-(c) but for temperature (K). Black contours on the non-convective plots are lines of constant conditional risk. 39

2.10 2D histogram of bootstrapped mean relative risk as a function of in-situ wind speed (m/s) and a) vertical distance from echo top and b) horizontal distance from 10dBz echo. 40

2.11 Same as Fig. 2.10 but for temperature instead of windspeed. 41

2.12 Same as Fig. 2.10 but using the matched vertical gradient in potential temperature (K/km) as a proxy for stability instead of wind speed. . . 42

2.13 Convective percentage (blue) and relative risk (red) as a function of solar hour, where 12 represents when the sun is the highest in the sky. Grey bars depict the number of convective observations during each solar hour. 43

2.14 Same as Fig. 2.13, but stratified by climatological season 44

Abstract

Atmospheric turbulence near thunderstorms represents one of the most persistent hazards in commercial aviation, yet the spatial extent, environmental controls, and storm-structural dependencies of this hazard remain incompletely understood. Current federal guidelines recommend maintaining at least 20 miles of lateral separation from convective storm boundaries, a threshold that growing evidence suggests substantially underestimates the true area of elevated risk. This thesis uses over 37 million automated in-situ eddy dissipation rate (EDR) observations from commercial aircraft, paired with high-resolution GridRad radar data, to construct a modern spatiotemporal climatology of turbulence near thunderstorms over the contiguous United States and to examine how storm characteristics modulate near-storm turbulence risk.

The southeastern United States emerges as the nation's primary turbulence-near-thunderstorms hotspot, with the Gulf Coast, northern Florida, and portions of Mississippi and Alabama exhibiting the highest convective percentages and shortest return intervals between moderate-or-greater (MoG) turbulence events. However, convective frequency alone proves insufficient to explain the observed turbulence distribution, as large-scale environmental factors including upper-level wind speed, temperature, and static stability each modulate the spatial reach and intensity of convectively induced turbulence. Winter emerges as the season of highest relative risk in storm-present environments despite exhibiting the lowest overall convective frequency, attributable to the stronger and more southerly positioned wintertime jet stream. A pronounced diurnal cycle is identified, with relative risk peaking during the overnight hours despite a concurrent decline in convective activity.

Chapter 1

Literature Review of Turbulence

1.1 Introduction

Atmospheric turbulence is a major issue for aircraft operations. In-flight encounters with turbulence can cause passenger injuries and millions of dollars of structural damage to the aircraft itself (Williams and Joshi, 2013), and if severe enough, can lead to schedule delays and broader air traffic management disruptions (Sharman, 2016). Pilots are routinely instructed to avoid areas where turbulence may be present, but the proper distance required to ensure safety does not guarantee avoidance. While many mechanisms can generate turbulence in the atmosphere, convection is among the most dominant sources of turbulence-related accidents (NTSB, 2021). Current federal guidelines recommend avoiding storm boundaries by approximately 20 miles, yet recent studies have shown that significant turbulence can extend well beyond this threshold (Hitchcock et al., 2025). Turbulence can also occur in environments devoid of storms or clouds entirely, rendering it invisible to onboard detection equipment (Jaeger and Sprenger, 2007). Together, these findings highlight not only a need to revisit federal avoidance guidelines, but also a deeper understanding of where and why turbulence forms near convective systems (Lane et al., 2012). This review synthesizes the current literature on atmospheric turbulence with an emphasis on turbulence in the vicinity of thunderstorms, motivating a spatiotemporal analysis of turbulence occurrence and its

environmental controls over the United States.

1.2 Motivation

On May 21st, 2024, 229 people at London Heathrow airport boarded a Boeing 777-300ER, one of the safest aircraft ever assembled, featuring a strengthened fuselage and wings (Norris, 2003). Near the end of the flight, the aircraft encountered severe turbulence over the Irrawaddy Basin in Myanmar and was forced to make an emergency landing short of its destination in Singapore. In a span of just 4.6 seconds, the aircraft dropped 178 feet, launching passengers who had not yet fastened their seatbelts violently through the cabin. Of the 229 onboard, 105 were injured, some sustaining traumatic brain injuries, others fractured vertebrae, and one passenger died. This is known as Singapore Airlines flight SQ321. Preliminary reports attributed the event to a convective updraft, undetected by the aircraft, underscoring how turbulence can strike even the most capable aircraft without warning.

Beyond aviation, turbulence has been an active area of research for decades, yet despite considerable progress, it remains an unsolved problem in both physics and atmospheric science. In part, this is because turbulence is an inherently chaotic, nonlinear phenomenon, one that interacts with its own momentum and energy to produce flow patterns that are difficult or impossible to predict analytically (Alert et al., 2022). Computationally, the challenge is equally significant, as turbulence models require time-dependent, nonlinear solutions to partial differential equations that are expensive to simulate. These difficulties are compounded in the atmosphere, where controlled conditions are rarely achievable. A further complication is the scale mismatch between where turbulence is generated and where it must be forecast: turbulent eddies form on scales of roughly 100 meters, while operational forecast domains such as the

CONUS span over 4,600 km (Kaplan et al., 2005). Even convection-permitting numerical weather models, with resolutions on the order of 1 km, cannot properly resolve these features. And even if resolution were not a limiting factor, gaps in our understanding of turbulence generation, particularly for convectively induced turbulence (CIT), would still constrain forecast accuracy. Developing a modern spatiotemporal climatology of turbulence near thunderstorms offers a path forward, providing a data-driven foundation for identifying regions of enhanced turbulence risk and informing both forecasting practices and avoidance guidelines.

1.3 History

The study of turbulence has a long and multidisciplinary history, rooted in foundational work in fluid mechanics before expanding into the atmospheric sciences. George Stokes was among the first to quantify turbulent behavior through his study of viscous fluids in the mid-19th century (Stokes, 1865), but it was Osborne Reynolds' 1883 pipe flow experiments, in which dyed water streams were used to observe the transition between flow regimes, that established turbulence as a distinct area of scientific inquiry (Reynolds, 1883). The dimensionless quantity Reynolds introduced to characterize this transition would become known as the Reynolds number, forming the conceptual basis for understanding the conditions under which turbulence arises.

By the early 20th century, the advent of powered flight brought practical urgency to turbulence research, driving its expansion into meteorology. Theoretical contributions from Ludwig Prandtl on boundary layers (Prandtl, 1928) and Andrey Kolmogorov's statistical turbulence theory (Kolmogorov, 1991) provided a scientific foundation for describing turbulent energy cascades, the process by which energy injected at large scales is transferred through a hierarchy of successively smaller eddies before being

dissipated as heat by viscosity. This framework for understanding energy transfer across scales remains central to atmospheric turbulence research today.

World War II proved an unlikely catalyst for atmospheric observation. Military radar systems were frequently obscured by rain and storms, leading to the recognition that radar could be repurposed to detect thunderstorms which were already known to produce turbulent conditions hazardous to aircraft. Simultaneously, aircraft such as the B-17 demonstrated the capability for sustained flight in the lower stratosphere, exposing a pressing need for observations and forecasting above 30,000 feet (Fahey et al., 2016). Together, these developments spurred systematic efforts to study turbulence throughout the atmospheric boundary layer and free atmosphere.

These developments culminated in the Thunderstorm Project, which marked a turning point in thunderstorm and atmospheric turbulence research. Funded by Congress and involving multiple agencies including the Weather Bureau and the Army Air Forces, the project systematically investigated thunderstorms and their associated turbulence through coordinated aircraft flights, surface observations, radar data, and radiosonde measurements (Byers and Braham, 1949). Key findings included the identification of the three-stage thunderstorm life cycle, cumulus, mature, and dissipating, and the association of convective turbulence with storm updrafts and downdrafts. The project also demonstrated the potential of radar as a tool for detecting storm features hazardous to aviation, laying the foundation for modern turbulence detection and avoidance strategies.

Also during this period, the International Civil Aviation Organization (ICAO) was established in 1947 as a specialized agency of the United Nations tasked with coordinating standards and recommended practices for international air navigation. Among its expectations was the routine submission of air reports (AIREPs), sometimes called pilot reports (PIREPs), from commercial pilots while en route. In practice, AIREPs

consisted of verbal radio transmissions describing observed weather conditions, which then had to be manually transcribed by air traffic controllers before being distributed to local meteorology offices (Fahey et al., 2016). This cumbersome process meant that many reports never reached distribution, and potentially hundreds of turbulence observations were lost. By the 1970s, onboard computers capable of automatically recording wind speed, direction, and temperature had become standard on most commercial aircraft, streamlining the AIREP process considerably. Turbulence intensity was also reported more frequently during this period, though without standardized metrics, these reports remained largely subjective, leaving accurate turbulence observations still few and far between.

In the decades that followed, advances in observational and computational tools transformed turbulence research. Radiosondes, wind profilers, Doppler radar, and eventually satellite-based remote sensing enabled detailed observations of turbulent structures across broader spatial and temporal scales (Fahey et al., 2016), while numerical weather prediction models incorporated turbulence parameterizations that advanced both process understanding and forecasting capability. Research into CIT intensified alongside growing recognition of its aviation safety implications, and studies of clear-air turbulence (CAT) associated with jet streams and mountain waves were extended to encompass convectively generated turbulence as well. Efforts to develop turbulence climatologies, particularly in regions of frequent convective activity, aimed to provide probabilistic frameworks for anticipating turbulence distributions. Studies such as Wolff and Sharman (2008) and Baek et al. (2024) have advanced understanding of CIT frequency and distribution, while convection-permitting simulations have shed light on the environments conducive to significant turbulence generation (Trier and Sharman, 2009). Nevertheless, gaps remain in our knowledge of the specific locations and conditions most favorable for CIT, and forecasting and avoidance capabilities con-

tinue to lag behind operational needs. Machine learning applications to existing CIT detection algorithms represent a promising avenue for closing these gaps and advancing toward safer aviation practices (Lee et al., 2023).

1.4 Types

Atmospheric turbulence manifests in many forms, each driven by distinct physical mechanisms and posing unique challenges to aviation and forecasting. One of the most well-understood is mountain wave turbulence (MWT), which results from the breaking of gravity waves above and downslope of mountainous terrain (Sharman, 2016). As winds are forced upward over mountain slopes, gravity waves can steepen with altitude due to decreasing atmospheric density, eventually approaching a critical level where they overturn and break (Strauss et al., 2015). Large eddy simulations (LES) have shown that this turbulence generation is driven primarily by mean shear in the flow over the terrain (Epifanio and Qian, 2008), and that stronger directional shear can produce turbulence even over more modest terrain (Guarino et al., 2016). MWT is particularly prevalent over the western United States, where the north-south orientation of the Rocky Mountains creates persistent aviation hazards.

Closer to the surface, low-level turbulence (LLT) within the planetary boundary layer (PBL) introduces additional risks, especially during takeoff and landing. Causes include convection, strong winds, low-level wind shear, frontal passages, and mechanical forcing from surface obstacles and rough terrain (Sharman, 2016). Wake turbulence from other aircraft is another notable source, as trailing vortices generated during takeoff and landing can pose risks at busy airports, particularly when a lighter aircraft follows a heavier one. Beyond aviation, LLT has meaningful implications for wind energy production, atmospheric transport, and wildland fire behavior, motivating continued

efforts to improve boundary layer turbulence forecasting (Muñoz-Esparza et al., 2018). The complex, microscale dynamics of the PBL make this a particularly challenging forecasting problem, and considerable emphasis has been placed on developing new modeling approaches capable of better resolving turbulence in this layer.

While MWT and LLT present meaningful challenges, turbulence is especially prevalent in the vicinity of convection and storm boundaries, a phenomenon commonly referred to as convectively induced turbulence, or CIT. The prevalence of CIT in accident-producing events is documented in Kaplan et al. (2005), which found that 86% of 44 accident-producing turbulence events over the United States occurred within 100 km of deep convection. Wolff and Sharman (2008) reported that 85% of pilot reports from within convective clouds resulted in moderate or greater (MoG) turbulence. More recently, Baek et al. (2024) applied a satellite-based CIT algorithm over the East Asian domain and found that 18% of all turbulence cases (quantified using EDR >0.1) were attributable to CIT. The Wolff and Sharman (2008) study examines spatial distributions of CIT using lightning flash data, which allows for more effective filtering of non-convective turbulence sources than is possible with reanalysis or numerical weather prediction (NWP) data alone, both of which are typically too coarse to resolve convective-scale features. Rather than relying on NWP output, their approach leverages pilot reports (PIREPs), which, despite well-known limitations in subjectivity and consistency across aircraft and pilots, prove sufficient for constructing relative distributions of turbulence occurrence. Their findings nonetheless underscore the need for continued methodological development in CIT climatology.

CIT is broadly divided into two categories: turbulence occurring inside cloud boundaries (in-cloud CIT) and turbulence occurring in the clear air nearby (near-cloud turbulence, NCT). In-cloud CIT is comparatively easier to detect, as improved remote sensing techniques can identify cloud boundaries with reasonable accuracy (Sharman

and Trier, 2019). The turbulence itself typically arises from large variations in vertical velocity within convective updrafts and overshooting tops, producing chaotic wind patterns capable of impacting aircraft (Kim and Chun, 2012). Lane et al. (2003) showed that as these updrafts collapse, horizontal vortex structures with convective instability can form and manifest as turbulence. In organized convective systems such as squall lines or mesoscale convective systems (MCSs), numerous updrafts and downdrafts may coexist within a small area, creating particularly hazardous conditions (Lane, 2016). While pinpointing the exact location of turbulence within these systems remains difficult, pilots are generally advised to avoid convective updrafts and cloud boundaries as a primary mitigation strategy.

The greater forecasting challenge arises when turbulence extends outside cloud boundaries into regions generally assumed to be safe (Lane et al., 2012). Convective systems are capable not only of generating turbulence internally, but of modifying the surrounding environment in ways that produce turbulence well beyond the storm boundary (Trier and Sharman, 2009). Though NCT is typically weaker than in-cloud CIT, it is considerably more dangerous in practice because it is largely undetectable by onboard equipment (Lane et al., 2012). Risk decreases with distance from the storm, but the decrease is more gradual than pilots or air traffic controllers might assume as moderate or greater turbulence remains twice as likely as background levels as far as 70 km horizontally from storm boundaries (Lane et al., 2012) and up to 7 km above echo top heights (Hitchcock et al., 2025). It is worth noting, however, that convective systems are capable of modifying their surrounding environment at considerably greater distances, modeling studies have demonstrated turbulence-favorable conditions more than 100 km from storm boundaries (Trier and Sharman, 2009), suggesting that the term near-cloud turbulence, while useful operationally, may not fully capture the spatial extent of convective influence.

Despite advances in both onboard instrumentation and remote sensing, the spatial and temporal resolution of current observations remains insufficient to fully characterize the microscale processes driving NCT (Kim and Chun, 2012). Recent work has begun to establish meaningful connections between observations and storm intensity, altitude, and ambient wind conditions, gradually improving our understanding of turbulence occurring far from storm boundaries (Hitchcock et al., 2025). Turbulence events that occur without warning or well outside established generation regions are of particular research interest, as they offer new insight into turbulence mechanisms and can inform the development of better forecast models.

1.5 Mechanisms

Atmospheric turbulence arises from four basic mechanisms: surface friction, vertical wind shear, gravity waves, and convection (Lester, 1993). Surface friction results from mechanical forcing as airflow encounters natural obstacles such as mountains or trees, or human-made structures like buildings and bridges (Sharman, 2016). The turbulent eddies that form in response vary in intensity depending on surface complexity, atmospheric stability, and the speed and direction of the wind (Lester, 1993). While surface friction is largely confined to the boundary layer, wind-driven processes also contribute to upper-level turbulence through vertical wind shear, the change in wind speed and direction with height. Vertical wind shear is ubiquitous in the atmosphere and has been shown to be associated with increased turbulence risk for aircraft (Hitchcock et al., 2025). When wind shear develops within a statically stable layer, it can also serve as a precursor to gravity wave formation, linking these mechanisms in ways that compound their individual effects.

Gravity waves represent another important pathway to upper-level turbulence.

They form when statically stable air is displaced vertically and buoyant forces act to restore it to its equilibrium position, producing an oscillation that propagates through the atmosphere and can be perceived as turbulence by aircraft (Lester, 1993; Sharman and Trier, 2019). When wave amplitudes grow sufficiently large, nonlinear processes cause the waves to steepen, overturn, and ultimately break, generating significant turbulent patches in the surrounding environment (Dörnbrack et al., 1995). Turbulence can also arise indirectly when multiple gravity waves of differing amplitudes are vertically stacked, as the resulting flow curvature can destabilize the local environment even in the absence of wave breaking (Lester, 1993).

Convection, the last of the four basic mechanisms, can both generate CIT directly and serve as a source of gravity waves. In a statically unstable environment, surface heating causes air parcels near the ground to become less dense than the air above, initiating free ascent through the atmosphere in structures commonly called thermals (Lester, 1993). In sufficiently moist environments, these thermals can develop into deep convective updrafts, producing towering cumulus clouds and, ultimately, thunderstorms. The most intense CIT tends to occur where gradients of vertical wind velocity are largest, near the edges of the updraft core, and turbulence severity scales with updraft strength (Honomichl et al., 2013). As storms mature, downdrafts develop and similarly generate turbulence through large vertical velocity gradients. In organized convective systems, updrafts and downdrafts can coexist within a small area simultaneously, compounding the hazard and creating particularly dangerous conditions for aviators (Lane, 2016).

CIT occurs either within convective structures or in the clear air surrounding them (Sharman and Trier, 2019). While in-cloud regions can be extremely turbulent, they are relatively straightforward to detect and avoid using onboard radar (Lane et al., 2012). The surrounding clear air, though generally less turbulent, poses a greater

practical hazard precisely because it is difficult to detect (Lane et al., 2012; Lane, 2016). Current federal guidelines recommend maintaining a horizontal distance of at least 20 miles (32 km) from storm boundaries (FAA, 2023), but recent studies suggest this threshold substantially underestimates the area at risk, as convective systems can modify their surrounding environment well beyond that distance (Trier and Sharman, 2009; Hitchcock et al., 2025). One primary pathway for this environmental modification is through convective outflow, including upper troposphere and lower stratosphere (UTLS) divergence, which alters the wind profile and static stability of the surrounding atmosphere. The divergent flow enhances vertical wind shear along its edges, while the associated subsidence and mixing locally reduce static stability, both jointly working to reduce the Richardson number (Ri). Values of Ri below 0.25 are generally indicitive of turbulent flow (Lane et al., 2003). Storm-generated outflows can produce sharp vertical wind shear layers that amplify turbulence in areas such as anvil edges and regions downstream of overshooting tops (Trier and Sharman, 2018).

Convection can also modify its surroundings through the generation of convective gravity waves, similar in behavior to those described above, but initiated specifically by convective forcing rather than general atmospheric displacement. These waves can potentially form when deep convection within an overshooting top intrudes into the statically stable air above the anvil, imparting upward momentum that drives vertically propagating gravity waves and creates conditions favorable for turbulence (Trier and Sharman, 2018). In some cases, moist air carried through the overshooting top produces visible cirrus plumes (Homeyer et al., 2017), but the influence of these waves is more often invisible to detection equipment, making the resulting turbulence particularly hazardous (Trier et al., 2012; Kim and Chun, 2012). Under certain conditions, these waves can transition from vertical to horizontal propagation when they become trapped upon reaching a critical level, the point at which the wave's phase speed matches the

background wind speed (Trier and Sharman, 2018). Once trapped, the waves are confined to a horizontal layer and can travel significant distances from the storm, modifying stability gradients and expanding the region at risk for turbulence well beyond the visible storm boundary.

When convective gravity waves overturn and break, they can produce significant patches of turbulence through several interacting processes. As waves propagate upward, decreasing atmospheric density causes their amplitudes to grow, eventually leading to steepening and overturning when vertical displacements exceed the vertical wavelength (Fritts and Alexander, 2003). Breaking can also occur at critical levels, where the wave's phase speed matches the background wind speed, triggering wave absorption or reflection and promoting shear instabilities (Booker and Bretherton, 1967). When wave-induced displacements sufficiently reduce static stability, overturning becomes likely, a condition commonly assessed using Ri. Nonlinear interactions such as wave-wave interference or ducted layer trapping can further amplify wave amplitudes, increasing the likelihood of resonance and turbulence generation (Kim and Chun, 2012). Collectively, these processes convert organized wave energy into turbulent motion, with consequences for both atmospheric structure and aviation safety.

Beyond these four basic mechanisms, larger-scale atmospheric conditions can also promote turbulence indirectly by triggering one or more of the processes described above. The breakdown of anticyclonic flow, for instance, can produce inertial instability when absolute rotation opposes planetary rotation, driving horizontal accelerations and enhanced wind shear (Bright et al., 2016). This breakdown can also generate gravity waves that propagate through the atmosphere and produce turbulence as described above. Jet streaks represent another large-scale feature of note, with exit regions particularly prone to intense gravity wave generation and subsequent turbulence intensification (Uccellini and Koch, 1987). Taken together, turbulence generation

is a multiscale problem, spanning the microscale dynamics of individual wave breaking events to the synoptic-scale flow patterns that set the stage for them, underscoring the difficulty of detection and forecasting and the continued need for research in this area.

1.6 Detection

Among the earliest metrics used to characterize turbulence is the Reynolds number (Re), a dimensionless quantity that describes the transition from laminar to turbulent flow by measuring the ratio of inertial to viscous forces (Bush, 2011). In the atmosphere, viscous forces rarely dominate as inertial forces are far more prevalent at typical atmospheric eddy scales, meaning Re is almost always high and turbulent flow is the norm rather than the exception (Sharman, 2016). While useful historically, the Reynolds number offers limited practical value for atmospheric turbulence detection, as it does not account for thermodynamic properties of the atmosphere. The Richardson number (Ri), developed later, addresses this by relating atmospheric stability to vertical wind shear. Values of Ri below 0.25 are generally indicative of turbulent flow, though turbulent activity can persist at values up to and beyond 1, with lower values associated with more severe turbulence (Miles, 1986; Storer et al., 2017). Because Ri incorporates direct measurements of atmospheric structure rather than purely fluid dynamic properties, it is considerably more useful than Re for detecting CAT in operational contexts (Gernowo et al., 2019).

Despite their utility, both Re and Ri are difficult to measure directly aboard aircraft, and neither accounts for the fact that a given turbulent environment will be experienced differently depending on the aircraft encountering it (Lester, 1993). Since the late 1990s, commercial aircraft in the United States have addressed this through automated in-situ recordings of the eddy dissipation rate (EDR), more precisely reported as the

cube root of the dissipation rate per unit mass (Sharman et al., 2014). Because EDR is related to the root-mean-square of aircraft vertical velocity and structural loads, it is aircraft-independent, making it a more consistent and transferable measure of turbulence intensity than pilot-reported metrics such as PIREPs, which suffer from subjectivity and inconsistency (Cornman, 2016). The improved fidelity and verifiability of automated EDR recordings have led the ICAO to adopt it as the standard metric for routine turbulence reporting.

Detecting and monitoring turbulence in real-time, commonly referred to as nowcasting, is critical for aviation safety. In-situ techniques employed by commercial aircraft provide the most direct measurements, with EDR serving as the primary metric given its aircraft independence and atmospheric interpretability (Sharman et al., 2014). However, in-situ observations are inherently limited to regions where aircraft are present, leaving large portions of the atmosphere unsampled.

Remote sensing techniques help address this gap and play an important complementary role in CIT detection. Doppler radar can identify turbulent motions within storm systems by measuring velocity variance among precipitation particles, while satellite-based infrared and visible imagery can detect convective cloud tops and gravity wave signatures that often precede CIT, providing broader spatial and temporal coverage (Bedka et al., 2010). Together, in-situ and remote sensing approaches offset one another's limitations, the former offering direct, localized measurements and the latter enabling wider coverage and earlier warning. Significant challenges nonetheless remain, particularly in improving the resolution and accuracy of CIT detection in clear-air regions far from convective sources, the areas where turbulence is hardest to anticipate and most dangerous to encounter.

1.7 Nowcasting/Forecasting

In the United States, the National Weather Service (NWS) issues two primary advisory products in response to forecasted or detected turbulence over the continental United States (CONUS). Significant Meteorological Information statements (SIGMETs) serve as severe weather advisories covering hazards relevant to all aircraft, including convection and severe turbulence, while Airman's Meteorological Information statements (AIRMETs) address less severe conditions such as low visibility or strong surface winds (Bright et al., 2016).

Turbulence forecasting at the operational level is supported by the World Area Forecast System (WAFS), established jointly by the World Meteorological Organization (WMO) and the ICAO to provide en-route guidance for aircraft operations. WAFS generates gridded upper-level wind and significant weather (SIGWX) forecasts multiple times daily, including 24-hour outlooks for jet streams, tropopause heights, and convection. These forecasts are provided at a resolution of 1.25° latitude by 1.25° longitude (roughly 85 by 85 miles) which far exceeds the scale at which turbulence actually occurs. As a result, direct turbulence forecasting at this resolution is not feasible, and meteorologists instead focus on identifying large-scale meteorological patterns associated with turbulence-generating mechanisms such as wind shear and frontogenesis, while also looking at forecasts for convection and turbulence parameters (Bright et al., 2016).

Historically, wind shear and frontogenesis were the large-scale features most commonly associated with turbulence, until deformation was identified as a third influential factor (Roach, 1970). This led Ellrod and Knapp (1992) to develop the Turbulence Index (TI), which forecasts turbulence in areas of large vertical wind shear and deformation. The TI correctly predicted between two-thirds and three-fourths of tur-

bulence events in their study, but showed notable deficiencies in non-frontogenetic environments. To address this, the divergence-modified turbulence index (DTI) was subsequently developed, incorporating divergence to better capture turbulence in situations where frontogenesis is absent, and outperformed the TI over the same study domain (Fahey et al., 2016).

The need for automated, real-time turbulence forecasting led to the development of the Graphical Turbulence Guidance (GTG) product, which blends gridded numerical weather prediction (NWP) data with a weighted combination of multiple turbulence diagnostics, including Ri, TI, and DTI to produce a more comprehensive representation of atmospheric turbulence than any single index could provide (Sharman et al., 2006). GTG outperformed individual diagnostic approaches, though its accuracy remained constrained by limited understanding of the relationship between aircraft-scale turbulence and NWP-resolvable features. Subsequent updates to the system, most notably the development of a statistical mapping method that relates turbulence diagnostics to EDR assuming a lognormal distribution of diagnostic values, yielded further improvements, particularly for MWT and CAT (Sharman and Pearson, 2017). Nevertheless, forecast skill remains bounded by gaps in our understanding of turbulence processes and by inherent errors in NWP model output.

While GTG has shown strong results for MWT and CAT, forecasting turbulence associated with convective clouds remains considerably more difficult due to the small-scale, transient nature of convection and the incomplete understanding of CIT generation mechanisms described above. A GTG-style blended approach is applied to CIT forecasting as well, though with much shorter achievable lead times. The most theoretically feasible strategy involves identifying background flow conditions and mesoscale features that would support intense turbulence should convection develop (Lane and Sharman, 2008), with relevant predictors including surface cyclogenesis, positively

tilted troughs, and upper-level cutoff lows (Bright et al., 2016). More recently, an EDR index was implemented in the European Centre for Medium-Range Weather Forecasts (ECMWF) integrated forecasting system (IFS) (Bechtold et al., 2021). This has been used by Gisinger et al. (2024) to retroactively forecast CIT for flight SQ321 (see section 1.1) in which they were able to predict the convection and associated turbulence 24 hours in advance, marking a huge step for the forecasting potential of CIT. Still, CIT forecasting remains one of the more stubborn challenges in operational meteorology, reflecting both the complexity of convective processes and the resolution limitations of current NWP systems.

1.8 Research Objectives

Turbulence research has come a long way since the foundational work of Stokes and Reynolds, with each successive advancement unlocking a new piece of a remarkably complex puzzle. Multiple generation mechanisms have been identified, from invisible gravity waves amplifying and breaking in the upper atmosphere to convective systems perturbing the environment well beyond their visible boundaries, and increasingly sophisticated tools have been developed for detecting and forecasting them. Yet the puzzle remains incomplete. The exceedingly small scales on which turbulence is generated, combined with its inherently nonlinear nature, make the resolution of even our best numerical models and observational networks too coarse. The subjective pilot reports that long formed the backbone of turbulence climatology are an imperfect foundation upon which to build a precise understanding of where and when turbulence occurs.

The widespread adoption of automated EDR reporting aboard commercial aircraft represents a meaningful shift in this landscape, replacing subjective accounts with ob-

jective, aircraft-independent measurements of turbulence intensity across an expansive and continuously growing observational network. This thesis leverages that record to interrogate the spatiotemporal distribution of turbulence risk in the vicinity of thunderstorms over the United States. Motivated by the gaps identified throughout this review, this thesis pursues the following research objectives and hypotheses.

Motivated by the gaps identified throughout this review, particularly the reliance of prior climatologies on subjective or coarsely resolved observations, and the incomplete understanding of how near-cloud turbulence extends beyond visible storm boundaries, this thesis pursues three primary objectives:

RO1 Construct a modern, observationally-grounded climatology of turbulence in the vicinity of thunderstorms over the contiguous United States using automated in-situ EDR observations, characterizing where this turbulence occurs most frequently and whether its spatial distribution simply mirrors the frequency of convection itself.

RO2 Characterize the seasonal and diurnal structure of near-storm turbulence risk, testing whether periods of peak convective activity correspond to periods of peak turbulence risk or whether the two diverge.

RO3 Investigate the extent to which large-scale environmental conditions, namely upper-level wind speed, temperature, and static stability, modulate the intensity and spatial reach of near-storm turbulence independent of storm presence alone.

Based on the literature reviewed above, several hypotheses guide this analysis:

H1 Turbulence near thunderstorms is hypothesized to be most frequent across the southeastern United States, consistent with prior PIREP- and lightning-based climatologies.

H2 Given the higher frequency of organized convection during spring across much of the central and eastern United States, spring is hypothesized to exhibit the highest overall risk of turbulence near thunderstorms.

H3 Environments with greater static stability near the tropopause are hypothesized to support turbulence at greater distances from storm boundaries, consistent with more efficient gravity wave ducting and trapping.

H4 Both storm proximity and the surrounding large-scale environment are hypothesized to independently contribute to turbulence risk, such that neither storm presence nor environmental conditions alone will be sufficient to explain the observed spatial and temporal patterns of near-storm turbulence.

Chapter 2

A Climatology Of Turbulence Near Thunderstorms Over The United States

2.1 Introduction

Chapter 1 established the physical mechanisms underlying convectively induced turbulence, including the tendency for turbulence to extend well beyond the visible storm boundary through gravity wave propagation, wave ducting near the tropopause, and outflow-driven reductions in the Richardson number. What remains poorly constrained is the observational picture: where across the United States this turbulence is most likely to be encountered, how that likelihood varies seasonally and diurnally, and whether its spatial distribution simply tracks the frequency of convection itself. Addressing these questions requires an observational climatology built at sufficient resolution and scale to isolate near-storm turbulence from other overlapping sources, motivating the analysis presented in this chapter.

Much of the existing literature focuses on convection as a turbulence-generating mechanism. The occurrence of turbulence near thunderstorms is inherently tied to the regional distribution of deep convection, which in turn is influenced by local topography

and synoptic-scale forcing. For example, Kaplan et al. (2005) reported that 38 of 44 turbulence-related aircraft accident cases in the United States (86%) occurred within 100 km of deep convection. In contrast, Proud (2015) found that only about 3% of commercial flights over Europe were within 35 km of convective activity. Similarly, Meneguz et al. (2016) identified convection as the source of 11% of moderate-or-greater (MoG) turbulence events over Europe. This proportion closely aligns with findings from Kim and Chun (2012), who reported that 11% of MoG turbulence over Korea was attributable to convection. These regional discrepancies underscore the variability in turbulence near thunderstorm prevalence across different geographic domains and highlight the need for spatially resolved climatological analyses.

Other studies have attempted to diagnose the spatial distribution of atmospheric turbulence using reanalysis products. Jaeger and Sprenger (2007) used a suite of clear-air turbulence (CAT) diagnostics, including the Richardson number (Ri) and the empirical Turbulence Index (TI) developed by Ellrod and Knapp (1992), to map CAT frequency across the Northern Hemisphere using ERA-40. Their approach benefited from a global dataset, but the relatively coarse horizontal resolution of the product (90 km $\times$ 90 km horizontal spacing) limited the fidelity of turbulence identification. More recently, Lee et al. (2023) revisited this diagnostic framework using the higher-resolution ERA5 (30 km $\times$ 30 km horizontal spacing). In addition to classical instability measures such as Ri, Lee et al. (2023) incorporated multiple versions of the Turbulence Index (TI1, TI2, TI3), expanding on earlier methodologies (Ellrod and Knapp, 1992). While these diagnostics have demonstrated reasonable skill in identifying regions with favorable environmental conditions for turbulence, they are not observations of turbulence occurrence. These climatologies nonetheless reveal coherent large-scale and seasonal patterns in turbulence-favorable environments.

In contrast to reanalysis-based approaches, Wolff and Sharman (2008) employed

PIREPs to construct a turbulence climatology over the continental United States. Unlike reanalysis-driven diagnostics, this study leveraged a long-standing, extensive observational dataset, enabling a more direct assessment of spatial patterns in observed turbulence. However, the use of PIREPs introduces several well-documented limitations. Notably, position errors in reported locations can exceed 50 km in the horizontal, and temporal uncertainties often surpass three minutes (Sharman et al., 2014). Furthermore, PIREPs are inherently subjective and aircraft-dependent, as reported turbulence severity varies with both pilot perception and airframe characteristics. Despite these constraints, Wolff and Sharman (2008) produced a broad depiction of turbulence occurrence across the U.S. Additionally, they correlated PIREPs with lightning flash data (a proxy for deep convection) to generate the first spatial estimates of turbulence near convection. Their findings indicated that this type of turbulence was most prevalent in the southeastern United States including states along the Gulf Coast, highlighting regional hotspots of convective turbulence risk.

This study extends prior observational investigations by using automated in-situ commercial airline eddy dissipation rate (EDR) data to analyze flight level turbulence occurrence over the United States. Maps of individual seasons are produced to investigate sub-annual trends in turbulence near thunderstorms. Additionally, the seasonal and diurnal risk of experiencing MoG turbulence are investigated in a storm-relative framework and linked to environmental factors.

2.2 Data and Methods

2.2.1 Data Sources

This effort utilizes automated, in-situ EDR observations from commercial aircraft. This method of analysis yields a dimensionally consistent, aircraft-independent measure of turbulence intensity, making it particularly well-suited for long-term, comparative analyses (Cornman et al., 2004; Meymaris et al., 2019). EDR is estimated from aircraft motion, specifically, vertical velocity or acceleration depending on the aircraft (Wingrove and Bach, 1994; Cornman et al., 1995). The peak and mean EDR value is recorded at one-minute intervals and automatically downlinked at user-specified intervals which are accurate to within at least 10 km and 1 min (Sharman et al., 2014).

In this study, turbulence severity is categorized using the 99.5th, 99.9th, and 99.99th percentiles of the EDR distribution, corresponding to thresholds of 0.16, 0.22, and 0.34 $m^{2/3} s^{-1}$, respectively, for light, moderate, and severe turbulence (as described in Hitchcock et al. (2025)). These percentile thresholds are consistent with the EDR thresholds used/found in other studies (Sharman and Pearson, 2017; Sharman and Trier, 2019; Trier et al., 2022). This study focuses on moderate or greater turbulence events, defined at times when EDR >0.22 $m^{2/3} s^{-1}$ (i.e., MoG turbulence threshold). The decision to use MoG reports, rather than light-or-greater (LoG) or severe-or-greater (SoG) thresholds, reflects a balance between capturing impactful turbulence events and maintaining a sufficient sample size for statistical assessment.

The dataset analyzed spans the period from 2009 to 2014 and contains over 37 million individual in-situ observations of EDR. As is typical with aircraft-based observational systems, spatial sampling is most dense along major commercial flight corridors, particularly those linking large metropolitan hubs. Fig. 2.1 shows the spatial distri-

bution of total EDR observation counts across the domain, independent of turbulence intensity, illustrating this sampling structure directly. Observation density is concentrated along a comparatively small number of established commercial flight corridors linking major hubs, with substantially sparser coverage over less-trafficked regions such as the northern Rockies or the northern Great Plains. Because turbulence can only be recorded where aircraft are present, this non-uniform sampling is an inherent constraint on the climatology developed here. Despite this, bins with low observations still carry hundreds of observations, giving us adequate sampling across our research domain.

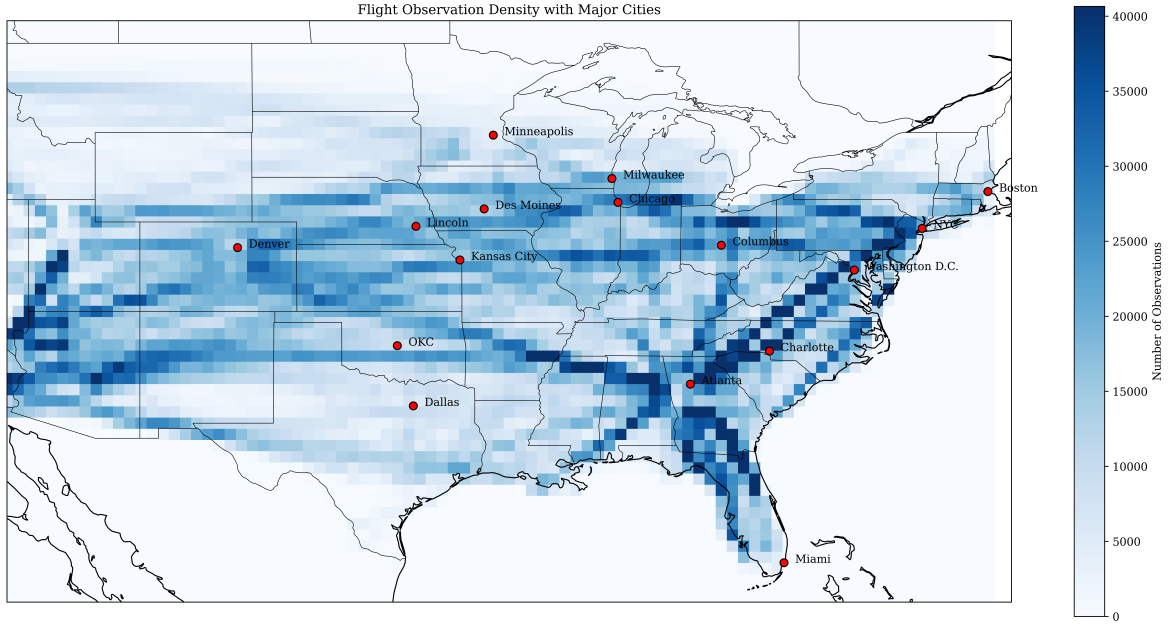

Figure 2.1: Number of EDR observations in each 0.5° x 0.5° bin from 2009-2014.

Additionally, observations below 8 km are excluded to remove any turbulence encountered during takeoff and landing. Along with this, we remove the influence of mountain wave turbulence by filtering out reports that meet all of the following criteria: (1) the report is >200 km away horizontally from storm boundaries, (2) its longitude is west of 104°W, and (3) has a reported EDR value of $>0.16 \mathrm{m}^{2/3}\,\mathrm{s}^{-1}$. These precautions are taken to ensure the analysis does not include any mountain wave turbulence that

is coincidentally in the vicinity of thunderstorms.

To isolate turbulence associated with thunderstorms, we incorporate gridded radar reflectivity data from the GridRad V3.1 (Homeyer and Bowman, 2017). GridRad aggregates volumetric radar observations from the NEXRAD WSR-88D network onto a high-resolution Cartesian grid (≈0.02° x ≈0.02° in longitude-latitude and 1 km in the vertical). This three-dimensional reflectivity field allows for detailed spatial and vertical analysis of convective structures. Data west of 115°W is not available in Gridrad V3.1, so it is not included in any analysis.

Convective storm objects are identified using a combination of echo-top height (ETH) and classification criteria. Specifically, storm regions are defined as regions with at least 4 contiguous points of defined echo tops (echo top heights defined similar to Cooney et al. (2018)) with an embedded area that has at least 4 points described as convective outlined by Steiner et al. (1995). More details can be found in Hitchcock et al. (2025). Once storm objects are defined, Hitchcock et al. (2025) calculated horizontal and vertical distances between reported turbulence and adjacent convective objects. These distance calculations form the foundation for the turbulence-convection proximity analyses presented in subsequent sections. It is important to note that horizontal distances are calculated between the aircraft and 10 dBZ reflectivity boundary. This does not represent the visible cloud edge and typically underestimates the full spatial extent of cloud material.

ERA5 reanalysis data from the European Centre for Medium-Range Weather Forecasts (ECMWF), with a native longitude-latitude resolution of $0.25° \times 0.25°$, 37 vertical pressure levels and a temporal resolution of an hour, is used to assess atmospheric static stability. Static stability is quantified using the vertical gradient of potential temperature and is calculated between vertically adjacent pressure levels at cruising altitude, which corresponds to 100, 200, and 300 hPa. Each EDR observation is assigned a static

stability value from the closest time, grid cell and pressure level. This represents the background state of the atmosphere near the storm objects we are analyzing, but not necessarily the effects of the storms on the background environment.

2.2.2 Climatological Metrics

To construct a climatology of turbulence near thunderstorms, several key diagnostic metrics are first defined. One measure used in this study is relative risk, which quantifies the ratio of the frequency of MoG turbulence within a specified subset to the corresponding background MoG turbulence frequency. For example, if a given bin exhibits a MoG turbulence frequency of 0.50, while the background frequency is 0.25, the relative risk in that bin would be 2.0, indicating that turbulence is twice as likely to occur given those conditions compared to the background environment. This can be expressed mathematically as:

$$RelativeRisk = \frac{\frac{\mathrm{MoG_{bin}}}{\mathrm{Total_{bin}}}}{\frac{\mathrm{MoG_{overall}}}{\mathrm{Total_{overall}}}} \tag{2.1}$$

In this formulation, $\mathrm{MoG_{bin}}$ denotes the number of MoG turbulence observations within a given bin, and $\mathrm{Total_{bin}}$ is the total number of observations in that bin. The denominator of the relative risk equation represents the background frequency of MoG turbulence, computed as the total number of MoG events divided by the total number of observations across all bins in the dataset. By definition, this denominator is equal to 0.001 (see Hitchcock et al. (2025) for more details). This metric identifies conditions with enhanced turbulence frequency by returning values greater than one where the local MoG rate exceeds the background rate.

In addition to relative risk, for each bin we calculate return intervals for MoG

turbulence events. This is computed by first determining the per-minute frequency of MoG reports within a given subset, equivalent to the numerator of the relative risk formulation. The reciprocal of this frequency yields the average time between successive MoG occurrences, which is then converted to hours for interpretability. The calculation is expressed mathematically as:

$$ReturnInterval = \frac{Total_{bin}}{60 * MoG_{bin}} \tag{2.2}$$

While return interval is useful for identifying regions where MoG turbulence occurs frequently, it does not by itself indicate whether the turbulence is near thunderstorms or not. To address this, we additionally compute convective percentage, defined as the proportion of MoG turbulence reports that occur in proximity to identified storm objects. This metric highlights regions where turbulence is often near storms, indicating that the turbulence itself is more likely associated with convection than other influences such as mountain wave breaking or shear turbulence. This is expressed mathematically as:

$$ConvectivePercentage = (\frac{MoG_{convective}}{MoG_{overall}}) * 100\% \tag{2.3}$$

To compute the convective percentage metric, we first define what constitutes being "near" storms, given in the equation as $\text{MoG}_{\text{convective}}$. This threshold is determined empirically by examining how relative risk varies as a function of horizontal and vertical distance from storm boundaries, as defined in Chapter 2.2.1. To find this, we adapted figures from Hitchcock et al. (2025) and determined that the relative risk of experiencing MoG turbulence falls below two times the background risk 70 km horizontally and 7 km vertically of a storm object. These findings are shown in Fig. 2.2 and for the purposes of this study we identify $\text{MoG}_{\text{convective}}$ events as MoG events that occur within the 70

km horizontal and 7 km vertical separations, including those within storms.

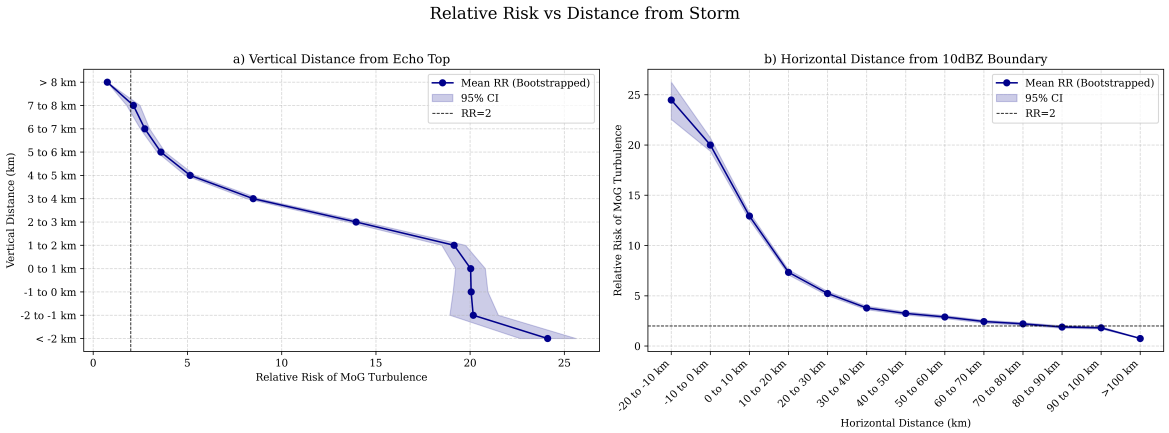

Figure 2.2: Relative risk (RR) as a function of a) vertical distance from echo top where negative distances denote within storm boundaries and b) horizontal distance from 10 dBZ boundary. Blue shading represents the 95% confidence intervals, and a dashed line is placed at RR=2.

2.3 Results

2.3.1 Turbulence as a Function of Distance From Storms

To assess the relationship between turbulence and convection, we first examine the frequency with which convection contributes to different intensities of turbulence. In Fig. 2.3 we see that as the EDR threshold increases, the proportion of reports occurring near convection rises monotonically, peaking at approximately 0.5 $m^{2/3} s^{-1}$, where nearly 45% of events fall within the 70 km horizontal and 7 km vertical proximity threshold. Beyond this point, particularly near 0.6 $m^{2/3} s^{-1}$, the convective percentage declines to approximately 40%. However, these high EDR values are rare within the dataset, limiting their influence on broader climatological patterns, as EDR values >0.5 $m^{2/3} s^{-1}$ only comprise approximately 0.03% of the entire dataset.

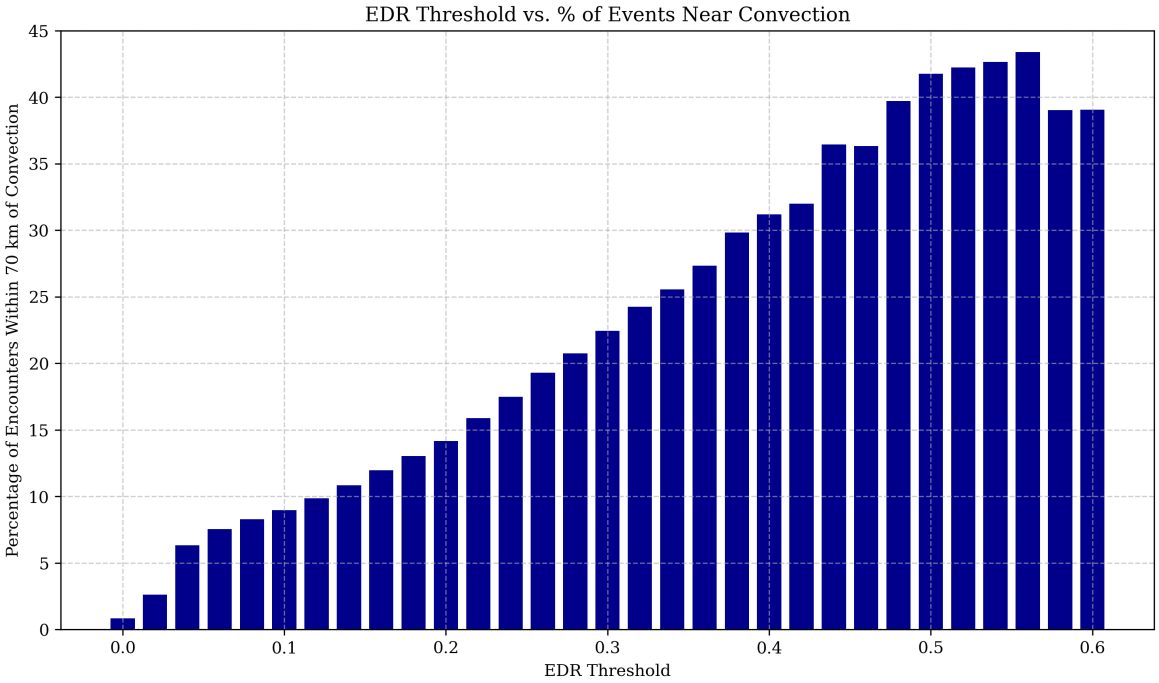

Figure 2.3: Convective percentage as a function of EDR threshold. Each threshold includes all observations in the dataset greater than that EDR threshold.

2.3.2 Spatial Patterns of Convection and Near Storm Turbulence Over the U.S.

Before investigating where near-storm turbulence occurs most frequently in the U.S., we investigate where convection itself occurs most often using GridRad. Figure 2.4a shows the highest number of storm objects is observed across the southern United States, with distinct maxima ranging from southern Illinois and Indiana extending south to the Gulf Coast. In contrast, lower storm frequencies are evident across the far northeastern U.S. and the Western Plains, particularly west of the Rocky Mountains. It is also true that the radar data in this region is coarser than that of the rest of the U.S., which would lead to lower fidelity of storm data over the Rocky Mountains. Despite this limitation, these regions match well with lightning flash density seen in Wolff and Sharman (2008).

The spatial patterns of convection established in this study serve as a reference point for evaluating the distribution of turbulence near thunderstorms. One central question is whether turbulence near thunderstorms simply mirrors the spatial frequency of convection, i.e., whether turbulence risk near storms is uniformly elevated regardless of geographic location. With this in mind, we can investigate convective percentages and return intervals to understand where in the US near-storm turbulence occurs, and whether or not their spatial patterns perfectly collocate with that of convection. Figure 2.4 shows that in the Gulf Coast and portions of the southeastern United States, convective percentages are largest, exceeding 50% in some areas, including Mississippi and Alabama. There is a secondary maximum in the northern Great Plains, with convective percentages closer to 30%. However, outside of these regions, most areas exhibit convective percentages between 10-20%, with percentages dropping to below 10% west of the Rocky Mountains.

This strong convective signal in the southeast is spatially collocated with the regions of low return interval observed in Fig. 2.4c, suggesting that this region also sees MoG turbulence often, with as few as 4 hours between MoG turbulence events. In contrast, areas such as the northern Great Plains and Rocky Mountains also exhibit short return intervals, but lower convective percentages, implying that non-convective mechanisms, such as jet streaks or mountain waves, are more often responsible for the more frequent turbulence in this region. High return intervals occur in the northeast and southwest United States, exceeding 18 hours. Note that the results in Figure 2.4c include all MoG reports regardless of their proximity to convection; as such, it reflects the broader climatological distribution of turbulence frequency rather than isolating convectively induced cases.

Comparison between all subplots in Fig. 2.4 suggests that while convective percentage is high in regions where convection often happens, there is some disconnect

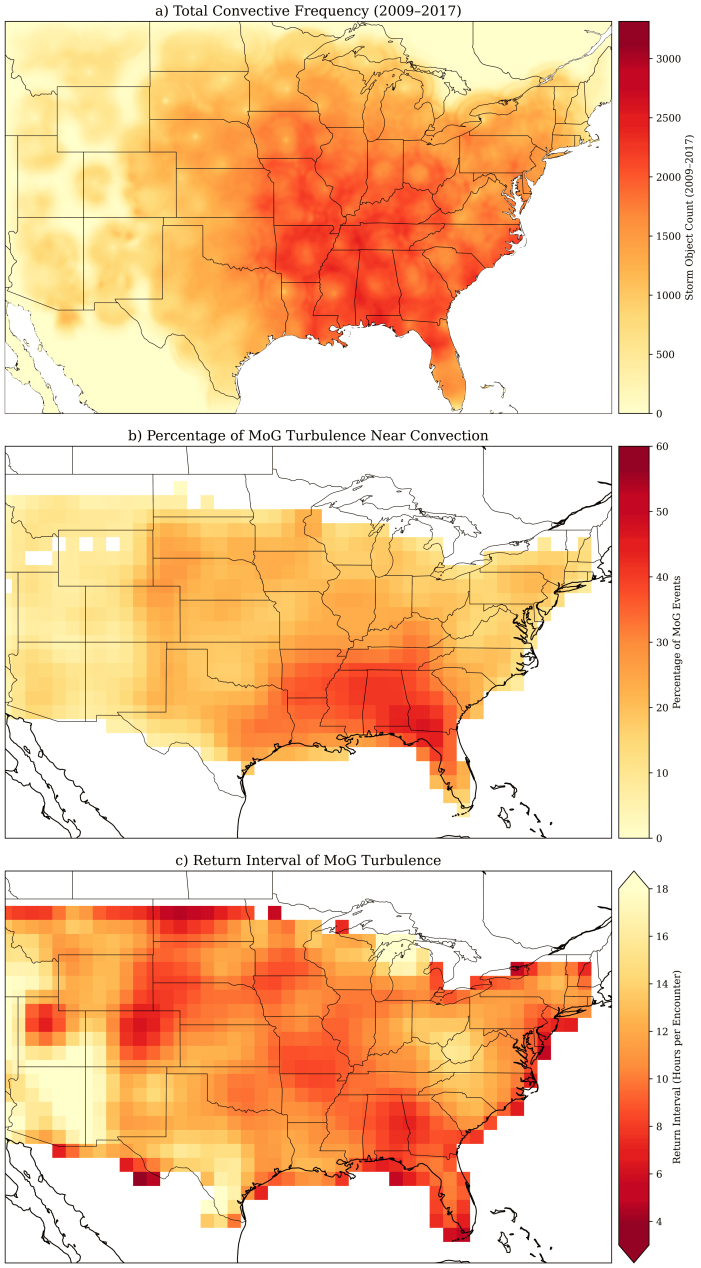

Figure 2.4: Spatial distribution of a) total storm objects over a 0.02° x 0.02° grid, b) convective percentage (%), and c) return interval of all MoG turbulence (hours) across the United States from 2009-2014 on a 1° x 1° grid. A Gaussian smoothing filter (sigma=5 for convective frequency, sigma=1 for other plots) has been applied to each plot.

between the occurrence of storms and near-storm MoG turbulence. Taken together, Fig. 2.4 identifies the southeastern United States as the primary region of most frequent

turbulence near thunderstorms, on average.

2.3.3 Seasonal Breakdown

In the following analyses, results from Chapters 2.3.1 and 2.3.2 are investigated as a function of season. Across both vertical and horizontal analyses, winter consistently exhibits the highest relative risk while summer shows the lowest (Fig. 2.5). Winter separates from spring around 2–3 km above the storm top and remains highest until 6–7 km, where all seasons begin to converge (Fig. 2.5a). Notably, even summer convection carries more than 10 times the background risk up to 2 km above the storm boundary. Winter and spring maintain elevated risk of MoG turbulence up to horizontal distances of 100 km, while risk in summer and fall diminish beyond approximately 70 km (Fig. 2.5b), providing further empirical justification for the 70 km proximity threshold used in this study. Inside storm boundaries, risk peaks for all seasons, with winter and spring reaching 30–40 times the background risk deep within convective structures, and summer retaining 10–20 times the background risk, a perhaps surprising result that will be discussed in further sections.

Spatial patterns are investigated through the same sub-annual lens. During winter, the highest storm frequencies remain concentrated in the southeastern U.S., though the spatial extent is more confined to coastal regions compared to the annual composite. This convection is well aligned with the convective percentage for the season, which is also confined to the southeast United States. Low return intervals cover a much greater extent, indicating frequent turbulence across most of the United States, including the southeast, where return intervals are as low as 5 hours between events. Similar to the annual composite, the southeast United States is the region of the most common turbulence near storms in winter.

In spring, the convective maximum shifts northwestward, with pronounced activity

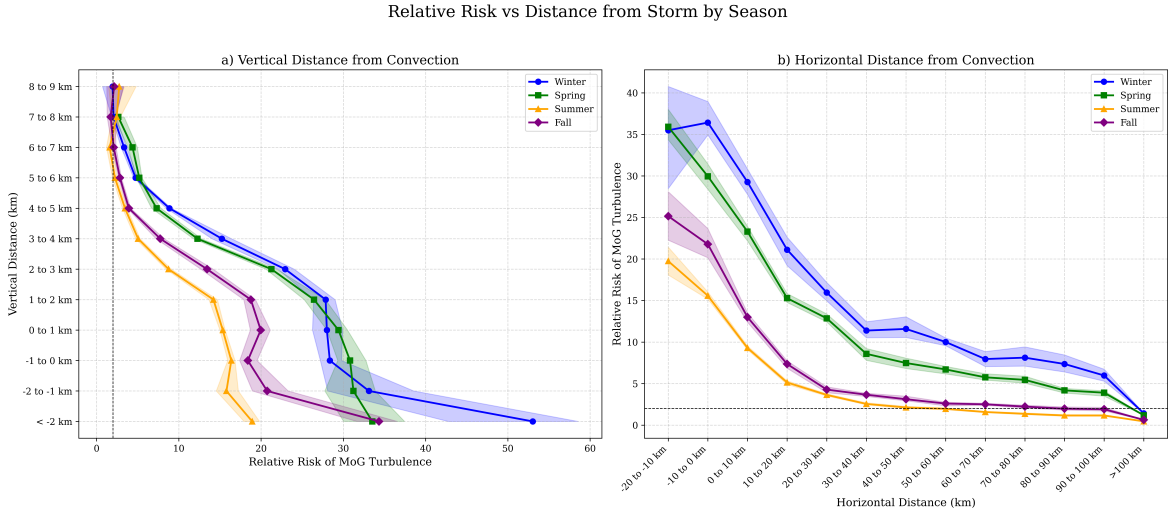

Figure 2.5: Bootstrapped relative risk as a function of a) vertical distance from echo top and b) horizontal distance from 10 dBz echo, where negative values are within storm boundaries. Results are stratified by climatological seasons (winter=DJF, spring=MAM, summer=JJA, fall = SON). Shading represents the 90% confidence intervals at each level. Dashed lines are marked at relative risk equal to 2.

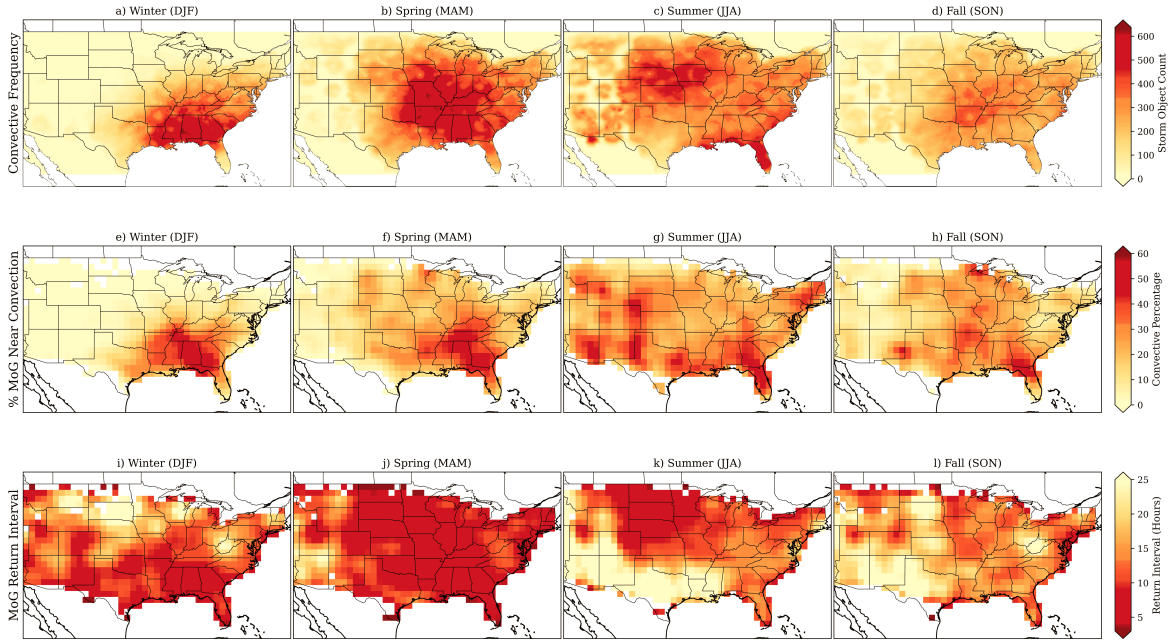

Figure 2.6: Seasonal spatial patterns of convective frequency (top row), convective percentage (middle row), and return interval of MoG turbulence (hours; bottom row). A Gaussian smoothing filter (sigma=5 for convective frequency, sigma=1 for other plots) has been applied to each plot.

over Arkansas and Missouri, while the Gulf Coast exhibits reduced activity compared to winter, though storms are still more frequent than other regions of the country. While convective percentage doesn't see as large of a shift, convection appears to have a larger influence than in the winter over a wider area. Return interval is low across much of the country outside of the southwest United States, indicating that spring has more uniform MoG turbulence. Still, because the overlap of higher convective percentage and low return interval is concentrated to the southeast United States, we conclude that turbulence near thunderstorms is still most common in the southeast during spring.

This northwestward migration of convective frequency continues into summer, with peak frequencies centered over Iowa and Nebraska. Notably, the extreme southern Gulf Coast and Florida also exhibit secondary maxima during this season, but the non-coastal regions of the states along the Gulf have relatively less convective activity compared to winter and spring. Despite this reduction of convective activity, we still find high convective percentages in the southeast United States, stretching along the southern portions of the country into New Mexico and Arizona, and stretching northward through the front range of the Rocky Mountains. Return intervals, on the other hand, are high in much of the southern United States in the summer, and reach their minimum in the northern Great Plains. This is partially collocated with high convective percentages, especially over western Colorado and eastern Nebraska, indicating this as the region of most common turbulence near thunderstorms. This represents the largest departure from the composite seen in Fig. 2.4.

By fall, the number of storm objects diminishes considerably, with a maxima located over Arkansas, indicating a seasonal decline in storm frequency relative to other times of the year. Convective percentage is also relatively low compared to other seasons, but, similar to summer, we still see the highest convective percentages in Arkansas and

northern Florida/southern Georgia. Return interval also reaches a maximum compared to other seasons. It minimizes just east of the northern Great Plains, peaking in southern Minnesota at around 7 hours between MoG turbulence events. Other peaks in return interval are observed in the southeast United States and Denver, but overall fall sees the lowest convective and turbulent activity.

2.3.4 Convective Influence on Turbulence Risk

While the preceding analyses have identified where turbulence near thunderstorms occurs most frequently across the United States, a fundamental question remains: do environments with storms inherently pose greater turbulence risk than environments without storms? To address this, we directly compare turbulence risk for reports within 70 km from a storm boundary (hereafter "LT70km") versus reports greater than 70 km from a storm boundary (hereafter "GT70km"). For each subset, the bin-wise MoG frequency within each population is calculated and then normalized by the overall background frequency across the entire dataset. Interpretation for this subset is slightly different from the relative risk metric used before, despite being computed similarly. Hereafter, this metric will be called a 'conditional risk.' This approach isolates the convective contribution to turbulence risk while controlling for baseline variability.

Fig. 2.7 presents the LT70km vs. GT70km comparison as a function of wind speed, building on findings from Hitchcock et al. (2025) that demonstrated a positive relationship between wind speed and turbulence occurrence near convection. Across all wind speeds, LT70km environments exhibit substantially elevated relative risk compared to GT70km conditions (Fig. 2.7a). At wind speeds below 10 m/s, LT70km conditional risk exceeds 35 times the background rate, whereas GT70km environments remain near 3 times background. While the LT70km case has much greater risk overall the condi-

tional risk rises at approximately the same rate for the GT70km case. Still, the lowest conditional risk in LT70km environments (which occurs at the lowest wind speed) is greater than the highest risk in GT70km environments. This demonstrates that proximity to active convection fundamentally alters turbulence risk independent of wind conditions alone. The percent difference (Fig. 2.7b) shows that LT70km environments exhibit 8–11 times higher risk at low wind speeds (<10 m/s), decreasing to 6–7 times at higher wind speeds (>20 m/s), with storm proximity consistently amplifying risk by at minimum 5.5-fold across all conditions.

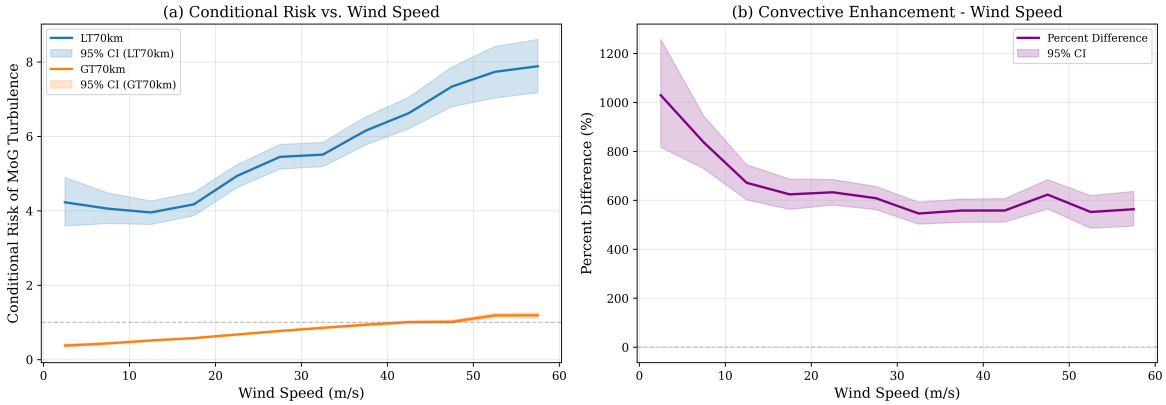

Figure 2.7: (a) Relative risk of MoG turbulence vs wind speed stratified by convective (<70 km from 10 dBZ boundary) and non-convective (>70 km from 10 dBZ boundary) and (b) percent difference between convective and non-convective environments. Shaded areas represent the 95% confidence intervals after bootstrapping.

The fundamental pattern that increasing conditional risk with wind speed and elevated values in LT70km environments relative to GT70km conditions holds across all seasons, notable differences emerge in the magnitude of convective risk. GT70km conditional risk remains nearly invariant across seasons, whereas LT70km environments exhibit some seasonal variability (Fig. 2.8). Contrary to the distance-based seasonal analysis (Chapter 2.3.3), which identified summer as the lowest-risk season, spring displays the lowest conditional risk across all wind speeds when controlling for wind conditions. The consistently lower spring values across the wind speed spectrum sug-

gest that, despite spring's elevated overall turbulence frequency (Chapter 2.3.3), the enhancement attributable specifically to convective proximity is smaller during this season compared to other times of year.

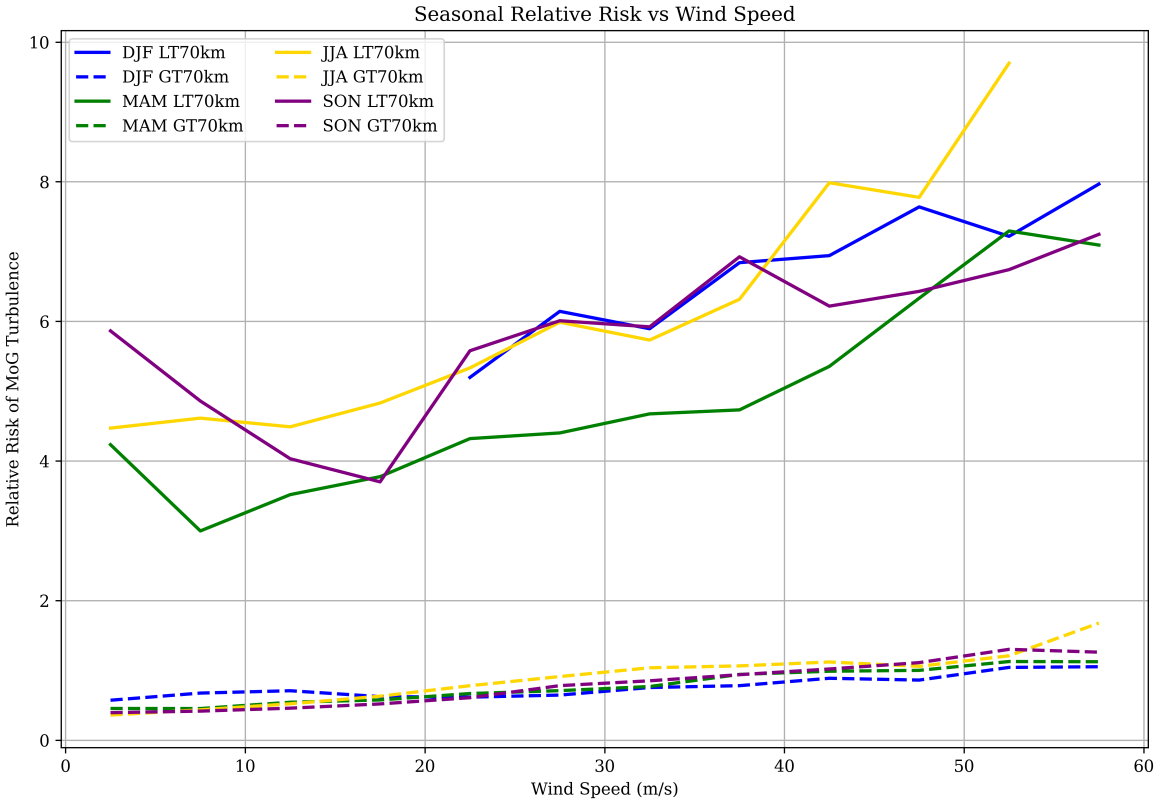

Figure 2.8: The same as Fig. 2.7a, but stratified by season. Due to limited sampling of wintertime convection in weak wind environments, winter data are only presented for wind speeds exceeding 20 m/s.

Fig. 2.9 extends this analysis as a function of altitude and to additional variables (in-situ temperature, ERA5 stability). It is important to note that observational coverage is limited to typical cruise altitudes, particularly in LT70km environments where aircraft maintain greater separation from storm tops. In both LT70km and GT70km environments, increases in wind speed have a greater impact on turbulence risk at lower altitudes; however, the difference in risk between the two environments is more pronounced at higher altitudes. The percent difference field (Fig. 2.9c) reveals that

a storms enhancement is greatest at higher altitudes with weak winds, reaching approximately 1600% (a 17-fold increase) near 11 km with wind speeds below 15 m/s. Even in regimes where the percent difference is minimized, high wind speeds at low-altitudes, a nearby storm still enhances relative risk by at least 200-400% (a 3-5 fold increase). These results demonstrate that proximity to storms substantially elevates turbulence risk across the full range of cruise altitudes and wind conditions encountered in commercial aviation.

LT70km environments exhibit peak conditional risk at stability values between 8-10 K/km and altitudes below 10 km, consistent with conditions near the tropopause where wave ducting is likely favored (Fig. 2.9d). Conditional risk generally decreases toward both lower stability values and higher altitudes. GT70km environments display substantially lower relative risk across all stability and altitude bins, with maximum values remaining below 5 times background, nearly an order of magnitude lower than LT70km conditions at equivalent stability (Fig 2.9e). A notable secondary peak of static stability is found at lower stability, denoted by the black contours. The percent difference field reveals LT70km enhancements exceeding 3000% (a 31-fold increase) at lower stability values (4-5 K/km), where GT70km baseline risk is minimal (Fig. 2.9f). Temperature exhibits similar patterns, with maximum relative risk at the lowest temperatures ($\sim$-55°C) in both environments, where impacts near storms are approximately 1100% more (12-fold increase) than those far from storms.

2.3.5 Environmental Modulation of Turbulence Near Thunderstorms

Having established that while environmental factors themselves can increase risk, the effect of convection is greater (Section 2.3.4), this section examines how environmental

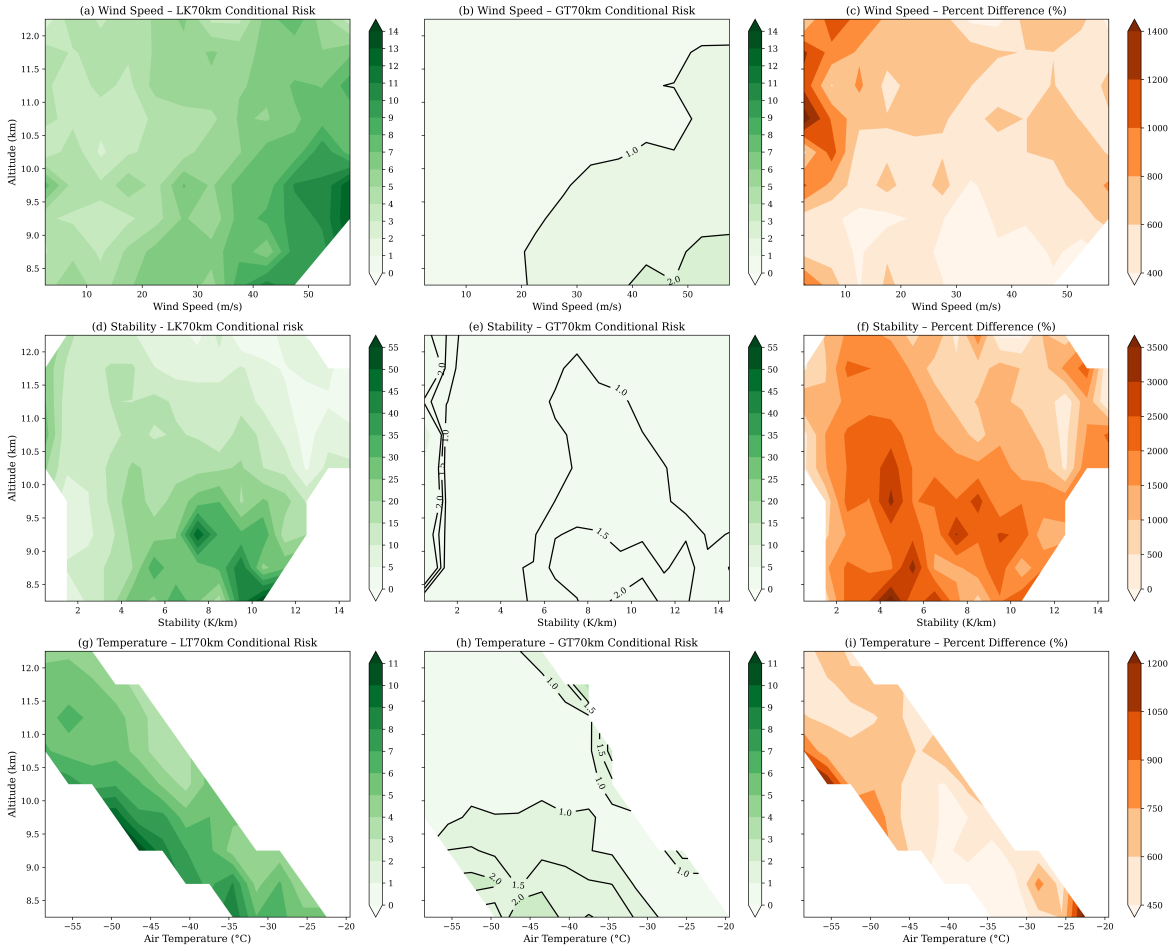

Figure 2.9: 2D histogram of (a) wind speed (m/s) vs altitude (km) filled with conditional risk in LT70km environments, (b) same as (a) but in GT70km environments, (c) the same as (a) but filled with percent difference between convective and non-convective environments, (d)-(f) the same as (a)-(c) but for stability (K/km), and (g)-(i) the same as (a)-(c) but for temperature (K). Black contours on the non-convective plots are lines of constant conditional risk.

conditions are related to the spatial structure of risk within convective domains beginning with in-situ wind speeds, which demonstrated the most pronounced convective enhancement in the preceding analysis. Relative risk increases with wind speed across all vertical distances from storm tops, with peak values occurring 1-2 km above the echo top at wind speeds of 60-65 m/s. Because in-situ sampling is concentrated outside storm boundaries, where aircraft can safely operate, the observed maximum occurs

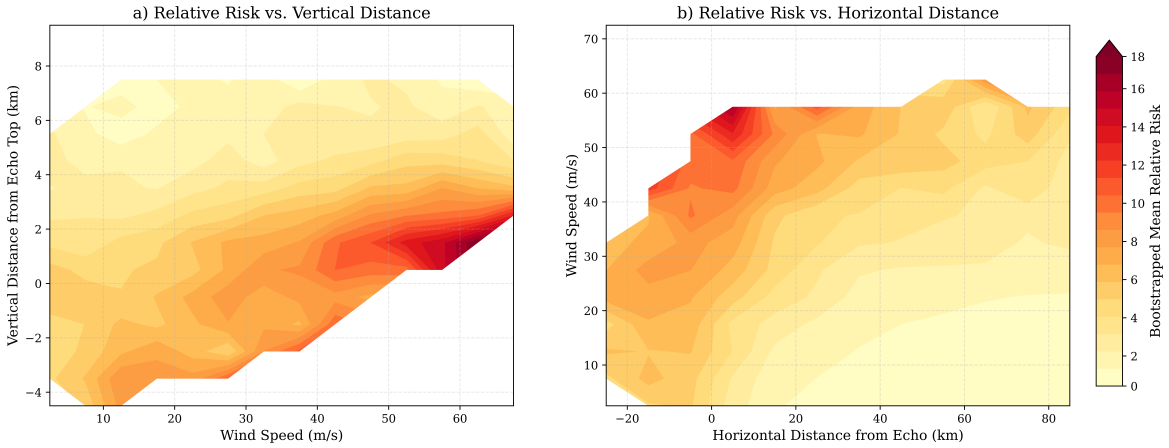

Figure 2.10: 2D histogram of bootstrapped mean relative risk as a function of in-situ wind speed (m/s) and a) vertical distance from echo top and b) horizontal distance from 10dBz echo.

just beyond the storm edge; stronger in-storm winds would likely correspond to even greater risk if directly sampled. Similarly, at any given horizontal distance from storm boundaries, higher wind speeds are associated with elevated relative risk (Fig. 2.10b). While the approach and dataset had differences, these findings align with Hitchcock et al. (2025), who documented an increased risk of MoG turbulence as a function of average ERA5 flight level background environmental wind speeds at the location of the storm.

Temperature exhibits similar distance-dependent patterns within convective environments. Fig. 2.11a shows that relative risk is maximized at low temperatures near storm tops, particularly within 2 km above the echo top, where temperatures below -45°C correspond to relative risk exceeding 15 times background. At fixed vertical distance, relative risk decreases with increasing temperature, while at fixed temperature, relative risk decreases with increasing height above echo top, consistent with the vertical decay patterns documented in Hitchcock et al. (2025). The horizontal analysis (Fig. 2.11b) reveals a similar structure: within 40 km of storms, relative risk increases systematically with decreasing temperature, though this dependence weakens beyond 40

km as relative risk becomes more uniform across temperature bins. The concentration of elevated risk in cold, near-storm environments aligns with the enhanced convective risk observed at low temperatures in Section 2.3.4.

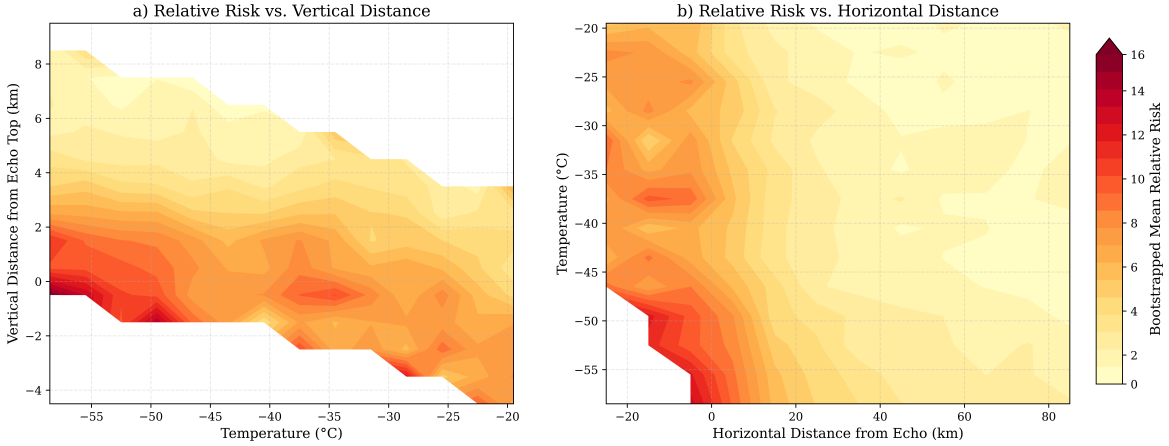

Figure 2.11: Same as Fig. 2.10 but for temperature instead of windspeed.

Static stability provides insight into wave ducting and gravity wave breaking processes that generate turbulence beyond visible cloud boundaries. Figure 2.12a shows that relative risk increases with stability within convective environments, reaching maximum values near 10 K/km, characteristic of the tropopause region (Tinney et al., 2022), and decreases with increasing vertical distance from storm tops, with this decay occurring more rapidly under strongly stable conditions. Beyond 4 km above the echo top, relative risk becomes nearly uniform across all stability regimes. The horizontal analysis (Fig. 2.12b) reveals that stability modulates the spatial extent of near-storm turbulence: under weak stability ($d\theta/dz \approx 2$ K/km), relative risk falls below 10 times background by approximately 15 km from storm boundaries, while under strongly stable conditions ($d\theta/dz \approx 10$ K/km), elevated relative risk persists beyond 70 km. Together, these results demonstrate that enhanced static stability, particularly near the tropopause, extends the horizontal reach of convectively induced turbulence while concentrating its vertical influence near storm tops, consistent with the elevated

convective enhancement observed at high stability in Section 2.3.4 (Fig. 2.9).

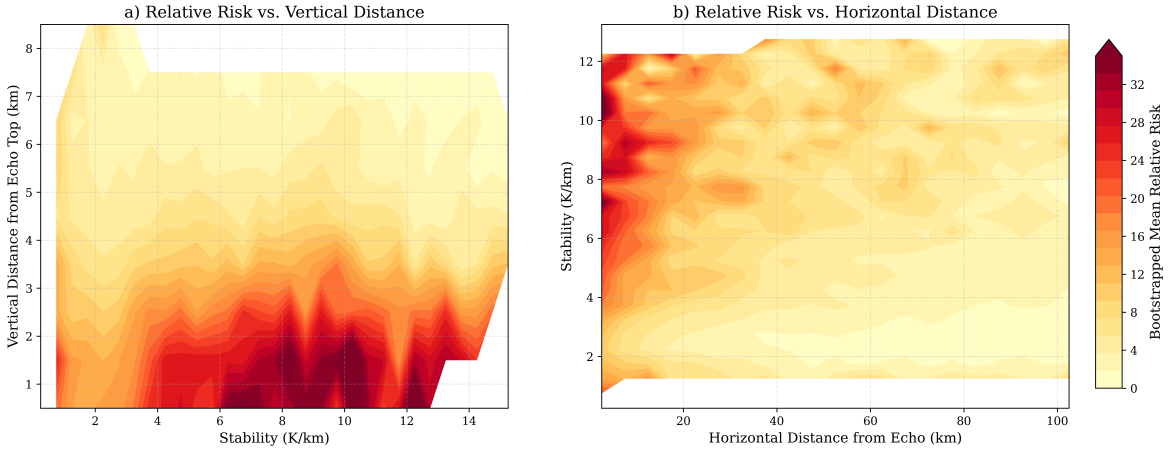

Figure 2.12: Same as Fig. 2.10 but using the matched vertical gradient in potential temperature (K/km) as a proxy for stability instead of wind speed.

2.3.6 Temporal Patterns in Turbulence Near Convection

A pronounced diurnal cycle emerges in convective percentage (Fig. 2.13), with values increasing steadily after noon and peaking between solar hours 17 and 18 (i.e., 5-6 p.m.), coinciding with typical convection initiation and growth during the late afternoon. In contrast, relative risk begins to rise slightly later, around solar hour 14 (2 p.m.), and continues increasing into the nighttime, reaching a maximum at solar hour 2 (2 a.m.). This relative risk peak occurs despite a concurrent minimum in convective percentage, as well as a drop in overall convective activity. The divergence between convective percentage and relative risk emphasizes that while convection contributes significantly to turbulence, it is not the sole driver of elevated risk. Other mechanisms, such as residual gravity waves or even non-meteorological factors, may play a stronger role during nocturnal hours.

Summer exhibits the clearest diurnal signal (Fig. 2.14), closely resembling the all-season pattern shown in Fig. 2.13. Convective percentage increases sharply after solar

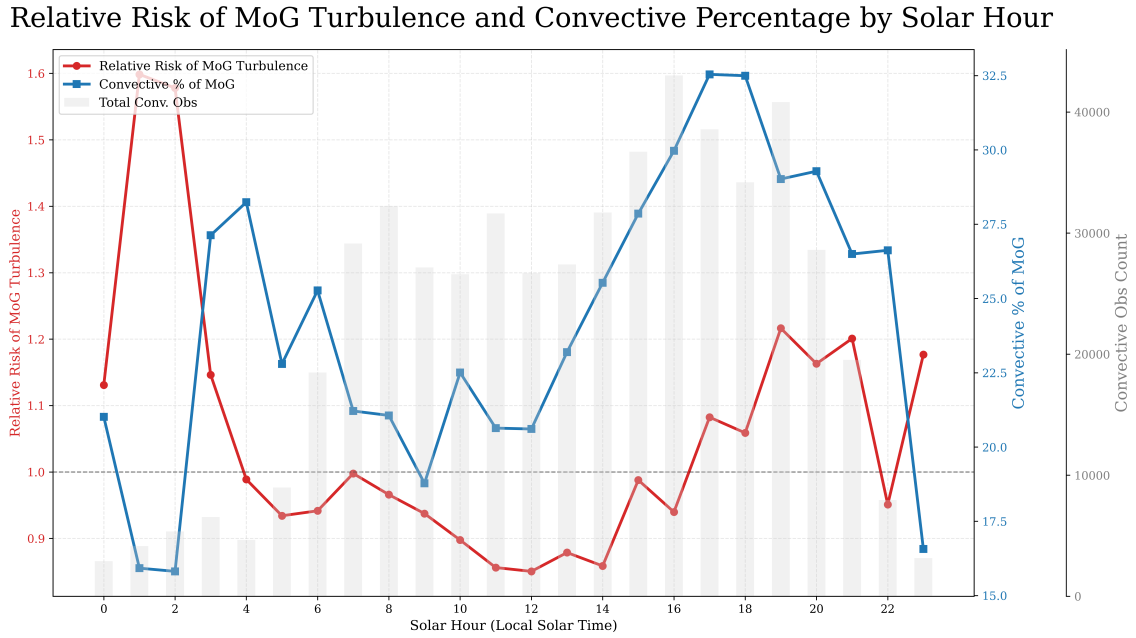

Figure 2.13: Convective percentage (blue) and relative risk (red) as a function of solar hour, where 12 represents when the sun is the highest in the sky. Grey bars depict the number of convective observations during each solar hour.

noon and peaks in the late afternoon to early evening, while relative risk follows with a delayed peak during the overnight hours around 2 a.m. Spring and fall also display moderate post-noon increases in convective percentage, although the signals are less pronounced than in summer. In both seasons, relative risk similarly lags behind convective percentage and reaches its maximum overnight. An anomalously high convective percentage signal appears during fall nighttime hours, which may be an artifact of low sample size, as nighttime convection is uncommon during this season. In contrast, winter shows minimal diurnal variability in either convective percentage or relative risk, suggesting that convective turbulence during this season is less influenced by time-of-day effects, or that a larger fraction of wintertime turbulence arises from non-convective sources that are themselves insensitive to diurnal forcing.

b) Seasonal Relative Risk and Convective Percentage by Solar Hour

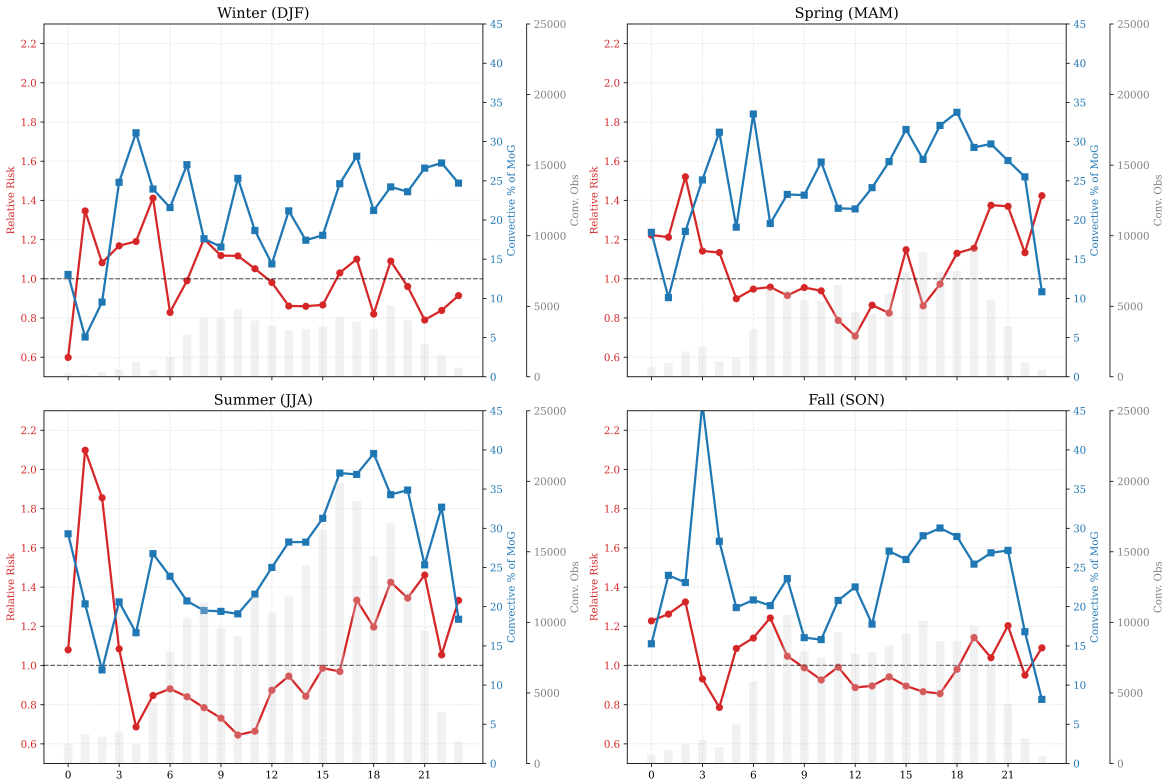

Figure 2.14: Same as Fig. 2.13, but stratified by climatological season

2.4 Discussion

2.4.1 Key Findings and Physical Interpretation

Taken together, the results of this study demonstrate that while deep convection is a major contributor to MoG turbulence, the occurrence of turbulence near thunderstorms is not determined by convective frequency alone. Instead, encounters with turbulence near active convection vary substantially across space and season, reflecting modulation by the surrounding large-scale environment. Regions and seasons characterized by stronger upper-level winds, lower temperatures, and enhanced static stability exhibit elevated relative risk and turbulence at greater distances from storm boundaries,

even where convection itself is less frequent. Conversely, regions of the US with frequent convective activity do not always correspond to higher proportions of turbulence near storms, indicating that storm presence alone is insufficient to explain observed geographical turbulence patterns. Direct comparison of LT70km versus GT70km environments confirms that while environmental factors modulate turbulence occurrence, proximity to active convection amplifies risk across all conditions examined, establishing storms as the dominant control on turbulence generation.

In several regions, turbulence is frequent despite relatively low convective association, suggesting that large-scale dynamical processes (e.g. jet streams / CAT) contribute more to turbulence occurrence in these locations. In addition, differences in storm organization and severity may modulate the apparent connection between convection and turbulence in the observational record, as aircraft routing decisions often lead to avoidance of the most intense convective systems. As a result, turbulence physically linked to convection may be underrepresented in the data in regions dominated by more organized storms. These effects vary seasonally: winter tends to exhibit a closer alignment between convection and turbulence when storms do occur, whereas spring and summer increasingly reflect a decoupling between convective activity and turbulence occurrence, when expansive organized convection is most common (Feng et al., 2019). This seasonal contrast motivates closer examination of the environmental conditions that govern when and where aircraft encounter turbulence near convection.

Winter emerges as the season with the highest relative risk in storm-present environments, despite exhibiting the lowest overall convective frequency. This behavior likely reflects the influence of the wintertime jet stream, which is both stronger and positioned farther south, producing enhanced upper-level wind speeds and increased static stability across much of the study domain (Hallam et al., 2022). These environments are also characterized by lower temperatures, consistent with proximity to

the tropopause, although at typical cruising altitudes the lowered winter tropopause can result in comparatively warmer conditions at flight levels. When convection does occur in this active regime, storms are embedded within environments that favor more intense and spatially extensive turbulence, allowing convective influences to extend far from storm boundaries.

Static stability emerges as a key environmental control on the spatial extent of turbulence near thunderstorms, particularly in regions near the tropopause. The observed increase in relative risk under strongly stable conditions is consistent with environments that support gravity-wave propagation away from convective sources. In these settings, gravity waves generated by deep convection can remain coherent over long distances before reaching critical amplitudes and breaking, allowing turbulent conditions to exist far from storm boundaries. This behavior provides a physical explanation for the elevated relative risk observed tens of kilometers from convection under strong stability, in contrast to weakly stable environments where turbulence risk decays more rapidly with distance. The sharper decline in relative risk above storm tops under highly stable conditions further suggests that wave-induced turbulence is within a confined vertical layer near the tropopause, beyond which wave energy dissipates or becomes less dynamically relevant. It then follows that strong static stability does not simply enhance turbulence intensity near storms, but alters the horizontal and vertical reach of convectively generated turbulence.

During the warm season, convective activity exhibits a pronounced late-afternoon maximum, consistent with surface heating and convection initiation (Naserikia et al., 2023), while relative risk peaks several hours later during the overnight period. The lag between when the most turbulence occurs near convection and when the relative risk is largest suggests that turbulence associated with convection is not confined to periods of active storm development, but can persist well after convection initiation

has finished, likely through mechanisms such as residual gravity waves propagating within a stable nocturnal environment. In contrast, winter exhibits minimal diurnal variability in both convective percentage and relative risk, indicating that turbulence near thunderstorms during this season is less tied to solar forcing and more strongly influenced by the ambient large-scale flow. The weak diurnal signal in winter is consistent with the dominance of strong upper-level winds and enhanced static stability, which can sustain turbulence generation and propagation independent of time-of-day effects. Together, these diurnal patterns reinforce the interpretation that warm-season turbulence near thunderstorms is modulated by convective timing, whereas cold-season turbulence reflects a fundamentally different, dynamically driven (i.e. non-convective) regime.

2.4.2 Comparison with Prior Studies

These results reinforce the broader understanding that storm-present environments significantly elevate turbulence risk, particularly for the most severe encounters, where just under 45% of the highest observed EDR cases are associated with nearby convective activity. This is consistent with prior work, though studies such as Kaplan et al. (2005) focused specifically on accidents and incidents, suggesting the true association between severe turbulence and convection may extend well beyond such extreme cases.

In addition to spatial comparisons, seasonal patterns in turbulence frequency align with findings from Sharman et al. (2014), who identified a pronounced springtime maximum accompanied by a secondary winter peak, consistent with earlier work by Jaeger and Sprenger (2007), Wolff and Sharman (2008), and Lee et al. (2023). Our results mirror these observations: Fig. 2.6 reveals a distinct spring minimum in return intervals across much of the domain, with summer and winter of comparable magnitude, reinforcing spring as the dominant turbulence season. This seasonal signal is

also evident when isolating turbulence near thunderstorms, with the southeast United States showing a springtime peak in both low return intervals and elevated percentage of encounters near convection, suggesting a concurrence of dynamic and convective factors favorable for turbulence generation in this season. When considering return interval alone without filtering for convective proximity, our findings also show partial alignment with Lee et al. (2023): during winter, a broad region of low return intervals across the southeastern United States corresponds with their elevated turbulence frequency identified by the Ri and TI3 indices, and in summer, both studies exhibit a northward shift in turbulence frequency. Perfect correspondence is not expected given the differing scopes, as CAT diagnostics often identify regions with environments conducive to turbulence, regardless of whether convection influenced the environment at a particular location.

Our observed spatial patterns of near-storm turbulence over the US show broad agreement with those reported by Wolff and Sharman (2008), who examined the relationship between turbulence and lightning flash density as a proxy for convective activity, defining turbulence near thunderstorms as occurring within 0.5 hours and 40 kilometers of one or more lightning flashes. Consistent with our findings, they identified the Gulf Coast as the primary hotspot, though some regional discrepancies exist, with their results showing lower frequency in Alabama and Georgia and higher frequency in Louisiana and Texas relative to ours. They also examined subannual variability using slightly different temporal periods (January-March, April-June, July-September, October-December) than the climatological seasons employed here, though reasonable comparisons can still be drawn. Both studies consistently identify the Gulf Coast as the winter hotspot, while seasonal disagreements emerge in other seasons. For example Wolff and Sharman (2008) report spring maxima over Colorado and the central Great Plains and and summer maxima over the Ohio River Valley. Our analyses instead in-

dicate a continued southeastern focus in spring and a western Great Plains maximum in summer. Also, during fall, Wolff and Sharman (2008) identify a shift in maximum turbulence toward Texas, while our results show broader activity over the Midwest. Any discrepancies likely stem from differences in temporal binning, data sources, and convection identification methods. Nevertheless, both studies show strong agreement during winter, suggesting that turbulence near thunderstorms patterns during this season are particularly robust across methodologies.

2.4.3 Methodological Limitations

This study contains several methodological limitations and underlying assumptions that merit discussion. First, the temporal scope is restricted to the years 2009-2014. While the dataset includes millions of observations within this period, the finite range limits the ability to assess long-term trends or changes in turbulence near thunderstorms patterns over time. As a result, the climatologies developed here represent a snapshot of turbulence near thunderstorms behavior during this specific interval, rather than a time-evolving analysis. Sensitivity testing, such as repeating analyses using subsets of the full record, yielded spatial patterns consistent with those presented in this paper, supporting the robustness of the results despite the limited temporal range. Nonetheless, extending the analysis with more recent data would allow for greater confidence in both the spatial and temporal stability of the observed patterns.

A second limitation concerns the spatial resolution of the turbulence analysis. Due to the non-uniform spatial distribution of EDR observations, particularly the concentration of flight activity along major corridors and near busy airspace, using a finer spatial grid introduces sampling artifacts. For instance, overly granular binning can result in turbulence patterns that simply reflect flight density rather than atmospheric dynamics. To mitigate this, a coarser $1^\circ \times 1^\circ$ grid was adopted to balance statisti-

cal stability and spatial interpretability. While this coarser scale effectively reveals broad regional patterns, it inherently sacrifices localized fidelity, potentially obscuring smaller-scale turbulence features such as localized mountain-wave activity or isolated convection-driven turbulence.

Stability should be interpreted as a general background stability as opposed to something directly measured at the time and location of each EDR report. The coarse grid spacing in the horizontal and vertical and the hourly time resolution means that it is not possible to represent fine scale details of atmospheric stability at the locations of reports.

Along with this, we must consider that the environmental variables examined here, wind speed, temperature, and static stability, were each considered largely in isolation, when in reality these fields co-vary; strong upper-level winds, for example, are frequently collocated with enhanced static stability near the tropopause, and disentangling their independent contributions to turbulence risk was beyond the scope of this analysis. Additionally, this study treats all convective storms identically regardless of their structure, organization, or evolutionary stage, a simplification that likely obscures meaningful variability in the turbulence risk that individual storms pose (see Chapter 3, Section 3.3). Finally, while GridRad provides a high-resolution three-dimensional radar mosaic, the resulting storm boundaries are ultimately a reflectivity-based proxy for convection and may not capture the full extent of the cloud material, or the associated turbulence-favorable perturbations, that a given storm generates.

2.4.4 Conclusions

With the increased availability of automated in-situ EDR data from commercial aircraft, it is now possible to develop a more comprehensive climatology of turbulence near thunderstorms across the United States. Improved understanding of turbulence

near thunderstorm hotspots and temporal patterns, can help inform future guidance and decisions, potentially reducing exposure to turbulence, enhancing passenger safety, and improving operational efficiency.

The primary findings from this study are summarized below:

1. The Southeastern United States emerges as the nation's most prominent turbulence-near-thunderstorms hotspot, particularly along the Gulf Coast and into northern Florida and southern Mississippi.

2. While broadly consistent with convective patterns, turbulence near thunderstorms exhibits distinct spatial and seasonal variations. This indicates that turbulence occurrence is not solely dictated by the presence of convection.

3. MoG reports co-occurred with lower temperatures and higher wind speeds measured by onboard sensors.

4. Increased static stability near the tropopause increases the horizontal distance over which MoG turbulence risk extends.

5. When storms are nearby, conditional risk is always higher than when storms are far away or absent.

6. Relative risk in winter is higher than in other seasons at both horizontal and vertical distances from storms, with the risk of MoG turbulence reaching nearly six times the background risk at a horizontal distance of 60 km and a vertical distance of 4 km from storm boundaries.

7. Turbulence near thunderstorms follows a clear diurnal cycle that is more prominent during the warm season.

Collectively, these results indicate that turbulence near thunderstorms arises from an interplay between convective processes and the larger-scale atmospheric environment in which storms are embedded. While regions of frequent convection often experience elevated turbulence risk, the efficiency with which convection generates turbulence varies substantially across space and season, reflecting the influence of background wind structure, static stability, and storm-environment interactions. This variability implies that certain environments are inherently more conducive to turbulence near thunderstorms, independent of convective frequency alone. Recognizing these distinctions is essential for interpreting climatological turbulence patterns and motivates further investigation into how storm structure, environmental flow, and observational sampling together shape the turbulence risk encountered by aircraft.

Chapter 3

Synthesis and Future Work

3.1 Synthesis of Findings

This thesis set out to build a modern, observationally-grounded climatology of turbulence near thunderstorms over the United States, to characterize its seasonal and diurnal structure, and to evaluate how large-scale environmental conditions modulate that risk independent of storm presence alone. Chapter 1 established the physical basis for this work: convectively induced turbulence arises not only within storm boundaries but well beyond them, as convective gravity waves propagate away from their source, encounter favorable ducting conditions near the tropopause, and break in response to locally reduced Richardson numbers. The modification of ambient wind and stability fields by convective outflow, identified in Chapter 1 as a key pathway by which storms extend their influence into nominally clear air, recurs as a physical explanation throughout the results of Chapter 2.

Chapter 2 evaluated each of the hypotheses laid out in Chapter 1's Research Objectives, with mixed results. Consistent with H1, the southeastern United States, and the Gulf Coast in particular, emerged as the dominant hotspot for turbulence near thunderstorms, agreeing with prior PIREP and lightning-based climatologies but now resolved with an aircraft-independent, high-resolution observational record. H2 was not supported: rather than spring, winter produced the highest relative risk in storm-

present environments despite exhibiting the lowest overall convective frequency. This result was unanticipated, though it could plausibly be attributable to the stronger and more equatorward wintertime jet stream, an explanation this thesis did not directly test and one that would require a targeted case-study or reanalysis-based investigation of individual wintertime events to confirm.

Consistent with H3, static stability correlated with the spatial extent of turbulence near storms, with elevated risk persisting to roughly 15 km under weak stability and beyond 70 km under strongly stable, tropopause-adjacent conditions. While this pattern is consistent with more efficient gravity wave ducting and trapping under stable conditions, this thesis characterized the statistical relationship between stability and turbulence extent rather than the underlying wave dynamics directly, and confirming the mechanism would require case studies pairing individual storm environments with wave-resolving model simulations or direct diagnosis of gravity wave activity in the observations. Finally, in support of H4, direct comparison of turbulence risk near and far from storm boundaries (Chapter 2.3.4) demonstrated that both storm proximity and the surrounding environment independently contribute to risk, with neither alone sufficient to explain the observed spatial and temporal patterns. Taken together, these results demonstrate that storm presence alone is an incomplete predictor of turbulence risk: the same storm, embedded in different environments, poses meaningfully different risk profiles.

The diurnal analysis added a dimension not anticipated in the original objectives. Relative risk peaked several hours after the late-afternoon maximum in convective activity, reaching its highest values overnight even as convective frequency declined. This lag suggests that turbulence-favorable conditions, possibly sustained by residual gravity waves propagating through a stabilizing nocturnal environment, can persist well after the storms that generated them have weakened or dissipated. This finding rein-

forces a theme that runs throughout this thesis: turbulence near thunderstorms is not merely a proxy for convective activity, but the product of an interaction between convection and the atmospheric environment it is embedded within, one that can outlast the convection itself.

3.2 Broader Context

These findings sit within a longer trajectory of turbulence research that began with Byers and Braham's Thunderstorm Project and has progressed through PIREP-based climatologies, reanalysis-driven diagnostics, and now automated in-situ observation. Each generation of this work has traded some limitation for another: PIREPs offered direct observation but suffered from subjectivity and poor positional accuracy. Reanalysis-based diagnostics like the Turbulence Index and Richardson number offered dynamical consistency but identified turbulence-favorable environments rather than turbulence itself. The EDR-based approach taken here inherits neither of these specific limitations, but it does inherit a different one: aircraft observe where aircraft fly, and the resulting climatology is necessarily shaped by commercial flight corridors rather than by atmospheric processes alone.

Beyond the turbulence literature specifically, these results speak to a broader pattern in mesoscale meteorology, that the most operationally relevant atmospheric hazards are rarely governed by a single variable in isolation. Just as convective mode, environmental shear, and instability jointly determine severe weather potential, this work shows that convective presence and the ambient wind, temperature, and stability fields jointly determine turbulence potential. The practical implication, echoed in Chapter 2's discussion, is that uniform avoidance thresholds such as the current 20-mile federal guideline are a reasonable first-order approximation but are unlikely

to be optimal across all seasons, regions, and synoptic environments. A stability or shear-aware avoidance framework, even a coarse one, could meaningfully improve on a purely distance-based rule without requiring storm-scale forecast skill that the field does not yet possess. Several methodological limitations inherent to this approach, spanning the observational record's temporal scope, spatial resolution, and treatment of storms as structurally uniform, are discussed in detail in Chapter 2.4.3, and directly motivate several of the future directions outlined below.

3.3 Future Work

The results of this thesis motivate several natural next steps. Foremost among these is an investigation of how the structural characteristics of a storm, rather than its mere presence, modulate the turbulence risk it produces. Storm size, elongation, orientation, and organizational mode are all plausible candidates for further amplifying or constraining the environmental modulation identified in Chapter 2, and preliminary work suggests that larger, more organized convective systems may extend their turbulence footprint considerably farther than isolated cells. A related and largely unexplored question is whether storm mode specifically, e.g., discrete cells, clusters, or mesoscale convective systems, produces systematically different turbulence signatures independent of storm size alone. Classifying storms by mode would allow this future work to move beyond geometry alone and toward a more physically complete picture of how storm organization governs the strength and reach of the turbulence-generating mechanisms described in Chapter 1, including gravity wave propagation, outflow-driven shear and stability changes, and turbulence generated within a storm's own circulation.

Beyond storm structure, additional synoptic-scale analysis, such as investigation of

deformation fields or proximity to jet streaks, could provide further insight into how specific large-scale dynamical features modulate turbulence near convective storms, complementing the wind, temperature, and stability variables already considered here. Extending the observational record beyond the 2009–2014 period used in this thesis would also allow future work to assess interannual variability and potential long-term trends in turbulence near thunderstorms, an assessment not possible with the current fixed six-year window.

Together, these directions aim to build directly on the climatological and environmental foundation established here, moving from documenting where and when turbulence near thunderstorms is most likely to occur toward explaining why a given storm, embedded in a given environment, produces the turbulence risk that it does.

Reference List

Alert, R., J. Casademunt, and J.-F. Joanny, 2022: Active Turbulence. *Annual Review of Condensed Matter Physics*, **13 (Volume 13, 2022)**, 143–170, https://doi.org/10.1146/annurev-conmatphys-082321-035957, URL https://www.annualreviews.org/content/journals/10.1146/annurev-conmatphys-082321-035957.

Baek, S.-H., J.-H. Kim, S.-H. Kim, Y. Lee, Y.-J. Noh, and S.-M. Lee, 2024: Characteristics of Convectively Induced Turbulence in East Asia Using Geostationary Korea Multi-Purpose Satellite-2A (GK-2A) and In Situ Aircraft Data. *Journal of Geophysical Research: Atmospheres*, **129 (24)**, https://doi.org/10.1029/2024JD041671, URL https://onlinelibrary.wiley.com/doi/abs/10.1029/2024JD041671.

Bechtold, P., M. Braumberger, A. Dörnbrack, L. Isaksen, and M. Leutbecher, 2021: Experimenting with a Clear Air Turbulence (CAT) Index from the IFS. text 874, ECMWF. https://doi.org/https://doi.org/10.21957/4l34tqljm, URL https://www.ecmwf.int/en/elibrary/81205-experimenting-clear-air-turbulence-cat-index-ifs.

Bedka, K., J. Brunner, R. Dworak, W. Feltz, J. Otkin, and T. Greenwald, 2010: Objective Satellite-Based Detection of Overshooting Tops Using Infrared Window Channel Brightness Temperature Gradients. *Journal of Applied Meteorology and Climatology*, **49 (2)**, 181–202, https://doi.org/10.1175/2009JAMC2286.1, URL https://journals.ametsoc.org/view/journals/apme/49/2/2009jamc2286.1.xml.

Booker, J. R., and F. P. Bretherton, 1967: The critical layer for internal gravity waves in a shear flow. *Journal of Fluid Mechanics*, **27 (3)**, 513–539, https://doi.org/10.1017/S0022112067000515, URL https://www.cambridge.org/core/journals/journal-of-fluid-mechanics/article/critical-layer-for-internal-gravity-waves-in-a-shear-flow/8D72D50D8C40AFCC668E7047B2300EEF.

Bright, D. R., S. A. Lack, and J. A. Sparks, 2016: A Summary of Turbulence Forecasting Techniques Used by the National Weather Service. *Aviation Turbulence: Processes, Detection, Prediction*, R. Sharman, and T. Lane, Eds., Springer International Publishing, Cham, 213–226, https://doi.org/10.1007/978-3-319-23630-8_10, URL https://doi.org/10.1007/978-3-319-23630-8_10.

Bush, J. W. M., 2011: SURFACE TENSION MODULE. *2011*, https://doi.org/10.1093/acprof:oso/9780199605835.003.0002.

Byers, H., and R. Braham, 1949: The Thunderstorm. Report of the Thunderstorm

project. Tech. rep., U.S. Govt. Printing Office, 287 pp. URL https://hdl.handle.net/2027/uc1.31822010301570?urlappend=%3Bseq=5.

Cooney, J. W., K. P. Bowman, C. R. Homeyer, and T. M. Fenske, 2018: Ten Year Analysis of Tropopause-Overshooting Convection Using GridRad Data. *Journal of Geophysical Research: Atmospheres*, **123 (1)**, https://doi.org/10.1002/2017JD027718, URL https://onlinelibrary.wiley.com/doi/abs/10.1002/2017JD027718.

Cornman, L., G. Meymaris, and M. Limber, 2004: An update on the FAA Aviation Weather Research Program's in situ turbulence measurement and reporting system.

Cornman, L. B., 2016: Airborne In Situ Measurements of Turbulence. *Aviation Turbulence: Processes, Detection, Prediction*, R. Sharman, and T. Lane, Eds., Springer International Publishing, Cham, 97–120, https://doi.org/10.1007/978-3-319-23630-8_5, URL https://doi.org/10.1007/978-3-319-23630-8_5.

Cornman, L. B., C. S. Morse, and G. Cunning, 1995: Real-time estimation of atmospheric turbulence severity from in-situ aircraft measurements. *Journal of Aircraft*, **32 (1)**, 171–177, https://doi.org/10.2514/3.46697, URL https://arc.aiaa.org/doi/10.2514/3.46697.

Dörnbrack, A., T. Gerz, and U. Schumann, 1995: Turbulent breaking of overturning gravity waves below a critical level. *Applied Scientific Research*, **54 (3)**, 163–176, https://doi.org/10.1007/BF00849114, URL https://doi.org/10.1007/BF00849114.

Ellrod, G. P., and D. I. Knapp, 1992: An Objective Clear-Air Turbulence Forecasting Technique: Verification and Operational Use. *Weather and Forecasting*, **7 (1)**, 150–165, https://doi.org/https://doi.org/10.1175/1520-0434(1992)007⟨0150:AOCATF⟩2.0.CO;2, URL https://journals.ametsoc.org/view/journals/wefo/7/1/1520-0434_1992_007_0150_aocatf_2_0_co_2.xml.

Epifanio, C. C., and T. Qian, 2008: Wave–Turbulence Interactions in a Breaking Mountain Wave. *Journal of the Atmospheric Sciences*, **65 (10)**, 3139–3158, https://doi.org/10.1175/2008JAS2517.1, URL https://journals.ametsoc.org/view/journals/atsc/65/10/2008jas2517.1.xml.

FAA, 2023: Aeronautical Information Manual. Tech. rep., Federal Aviation Administration. URL https://www.faa.gov/Air_traffic/publications/atpubs/aim_html/.

Fahey, T., E. N. Wilson, R. O'Loughlin, M. Thomas, and S. Klipfel, 2016: A History of Weather Reporting from Aircraft and Turbulence Forecasting for Commercial Aviation. *Aviation Turbulence: Processes, Detection, Prediction*, R. Sharman, and T. Lane, Eds., Springer International Publishing, Cham, 31–58, https://doi.org/

10.1007/978-3-319-23630-8_2, URL https://doi.org/10.1007/978-3-319-23630-8_2.

Feng, Z., R. A. Houze, L. R. Leung, F. Song, J. C. Hardin, J. Wang, W. I. Gustafson, and C. R. Homeyer, 2019: Spatiotemporal Characteristics and Large-Scale Environments of Mesoscale Convective Systems East of the Rocky Mountains. *Journal of Climate*, **32 (21)**, 7303–7328, https://doi.org/10.1175/JCLI-D-19-0137.1, URL https://journals.ametsoc.org/view/journals/clim/32/21/jcli-d-19-0137.1.xml.

Fritts, D. C., and M. J. Alexander, 2003: Gravity wave dynamics and effects in the middle atmosphere. *Reviews of Geophysics*, **41 (1)**, https://doi.org/10.1029/2001RG000106, URL https://onlinelibrary.wiley.com/doi/abs/10.1029/2001RG000106.

Gernowo, R., H. D. Saputro, A. Setiawan, K. Adi, and A. P. Widodo, 2019: Richardson number model for turbulence motion analysis around airport runway. *Journal of Physics: Conference Series*, **1217 (1)**, https://doi.org/10.1088/1742-6596/1217/1/012032, URL https://dx.doi.org/10.1088/1742-6596/1217/1/012032.

Gisinger, S., M. Bramberger, A. Dörnbrack, and P. Bechtold, 2024: Severe Convectively Induced Turbulence Hitting a Passenger Aircraft and Its Forecast by the ECMWF IFS Model. *Geophysical Research Letters*, **51 (23)**, https://doi.org/10.1029/2024GL113037, URL https://agupubs.onlinelibrary.wiley.com/doi/10.1029/2024GL113037.

Guarino, M.-V., M. A. C. Teixeira, and M. H. P. Ambaum, 2016: Turbulence generation by mountain wave breaking in flows with directional wind shear. *Quarterly Journal of the Royal Meteorological Society*, **142 (700)**, https://doi.org/10.1002/qj.2862, URL https://onlinelibrary.wiley.com/doi/abs/10.1002/qj.2862.

Hallam, S., S. A. Josey, G. D. McCarthy, and J. J.-M. Hirschi, 2022: A regional (land–ocean) comparison of the seasonal to decadal variability of the Northern Hemisphere jet stream 1871–2011. *Climate Dynamics*, **59 (7)**, 1897–1918, https://doi.org/10.1007/s00382-022-06185-5, URL https://doi.org/10.1007/s00382-022-06185-5.

Hitchcock, S. M., T. P. Lane, W. Deierling, R. D. Sharman, S. B. Trier, and C. R. Homeyer, 2025: Spatial Patterns of Turbulence near Thunderstorms. *Bulletin of the American Meteorological Society*, **106 (1)**, E1–E22, https://doi.org/10.1175/BAMS-D-23-0142.1, URL https://journals.ametsoc.org/view/journals/bams/106/1/BAMS-D-23-0142.1.xml.

Homeyer, C. R., and K. P. Bowman, 2017: Algorithm Description Document for Version 3.1 of the Three-Dimensional Gridded NEXRAD WSR-88D Radar (GridRad) Dataset. Tech. rep., University of Oklahoma, 23 pp. URL https://gridrad.org/pdf/

GridRad-v3.1-Algorithm-Description.pdf.

Homeyer, C. R., J. D. McAuliffe, and K. M. Bedka, 2017: On the Development of Above-Anvil Cirrus Plumes in Extratropical Convection. *Journal of the Atmospheric Sciences*, 1617–1633, https://doi.org/10.1175/JAS-D-16-0269.1, URL https://journals.ametsoc.org/view/journals/atsc/74/5/jas-d-16-0269.1.xml.

Honomichl, S. B., A. G. Detwiler, and P. L. Smith, 2013: Observed Hazards to Aircraft in Deep Summertime Convective Clouds from 4–7 km. *Journal of Aircraft*, **50 (3)**, https://doi.org/10.2514/1.C032057, URL https://doi.org/10.2514/1.C032057.

Jaeger, E. B., and M. Sprenger, 2007: A Northern Hemispheric climatology of indices for clear air turbulence in the tropopause region derived from ERA40 reanalysis data. *Journal of Geophysical Research: Atmospheres*, **112 (D20)**, https://doi.org/10.1029/2006JD008189, URL https://onlinelibrary.wiley.com/doi/abs/10.1029/2006JD008189.

Kaplan, M. L., A. W. Huffman, K. M. Lux, J. J. Charney, A. J. Riordan, and Y.-L. Lin, 2005: Characterizing the severe turbulence environments associated with commercial aviation accidents. Part 1: A 44-case study synoptic observational analyses. *Meteorology and Atmospheric Physics*, **88 (3)**, 129–152, https://doi.org/10.1007/s00703-004-0080-0, URL https://doi.org/10.1007/s00703-004-0080-0.

Kim, J.-H., and H.-Y. Chun, 2012: A Numerical Simulation of Convectively Induced Turbulence above Deep Convection. *Journal of Applied Meteorology and Climatology*, **51 (6)**, 1180–1200, https://doi.org/10.1175/JAMC-D-11-0140.1, URL https://journals.ametsoc.org/view/journals/apme/51/6/jamc-d-11-0140.1.xml.

Kolmogorov, A. N., 1991: The Local Structure of Turbulence in Incompressible Viscous Fluid for Very Large Reynolds Numbers. *Proceedings: Mathematical and Physical Sciences*, **434 (1890)**, 9–13, URL https://www.jstor.org/stable/51980.

Lane, T., 2016: Processes Underlying Near-Cloud Turbulence. *Aviation Turbulence: Processes, Detection, Prediction*, R. Sharman, and T. Lane, Eds., Springer International Publishing, Cham, 317–333, https://doi.org/10.1007/978-3-319-23630-8_16, URL https://doi.org/10.1007/978-3-319-23630-8_16.

Lane, T. P., and R. D. Sharman, 2008: Some Influences of Background Flow Conditions on the Generation of Turbulence due to Gravity Wave Breaking above Deep Convection. *Journal of Applied Meteorology and Climatology*, **47 (11)**, 2777–2796, https://doi.org/10.1175/2008JAMC1787.1, URL https://journals.ametsoc.org/view/journals/apme/47/11/2008jamc1787.1.xml.

Lane, T. P., R. D. Sharman, T. L. Clark, and H.-M. Hsu, 2003: An Investigation of Turbulence Generation Mechanisms above Deep Convection. *Journal of the Atmospheric Sciences*, 1297–1321, URL https://journals.ametsoc.org/view/journals/atsc/60/10/1520-0469_2003_60_1297_aiotgm_2.0.co_2.xml.

Lane, T. P., R. D. Sharman, S. B. Trier, R. G. Fovell, and J. K. Williams, 2012: Recent Advances in the Understanding of Near-Cloud Turbulence. *Bulletin of the American Meteorological Society*, **93 (4)**, 499–515, https://doi.org/10.1175/BAMS-D-11-00062.1, URL https://journals.ametsoc.org/view/journals/bams/93/4/bams-d-11-00062.1.xml.

Lee, J. H., J.-H. Kim, R. D. Sharman, J. Kim, and S.-W. Son, 2023: Climatology of Clear-Air Turbulence in Upper Troposphere and Lower Stratosphere in the Northern Hemisphere Using ERA5 Reanalysis Data. *Journal of Geophysical Research: Atmospheres*, **128 (1)**, https://doi.org/10.1029/2022JD037679, URL https://onlinelibrary.wiley.com/doi/abs/10.1029/2022JD037679.

Lester, P. F., 1993: *Turbulence : a new perspective for pilots*. Englewood, CO : Jeppesen Sanderson Training Systems, URL http://archive.org/details/turbulencenewper0000lest.

Meneguz, E., H. Wells, and D. Turp, 2016: An Automated System to Quantify Aircraft Encounters with Convectively Induced Turbulence over Europe and the Northeast Atlantic. *Journal of Applied Meteorology and Climatology*, **55 (5)**, 1077–1089, https://doi.org/10.1175/JAMC-D-15-0194.1, URL https://journals.ametsoc.org/view/journals/apme/55/5/jamc-d-15-0194.1.xml.

Meymaris, A. G., A. R. D. Sharman, A. L. Cornman, and A. W. Deierling, 2019: The NCAR In Situ Turbulence Detection Algorithm. Tech. rep., NCAR, 53 pp. https://doi.org/https://doi.org/10.5065/g24q-ea27, URL https://opensky.ucar.edu/islandora/object/technotes%3A580.

Miles, J., 1986: Richardson's criterion for the stability of stratified shear flow. *The Physics of Fluids*, **29 (10)**, 3470–3471, https://doi.org/10.1063/1.865812, URL https://doi.org/10.1063/1.865812.

Muñoz-Esparza, D., R. Sharman, J. Sauer, and B. Kosović, 2018: Toward Low-Level Turbulence Forecasting at Eddy-Resolving Scales. *Geophysical Research Letters*, **45 (16)**, https://doi.org/10.1029/2018GL078642, URL https://onlinelibrary.wiley.com/doi/abs/10.1029/2018GL078642.

Naserikia, M., M. A. Hart, N. Nazarian, B. Bechtel, M. Lipson, and K. A. Nice, 2023: Land surface and air temperature dynamics: The role of urban

form and seasonality. *Science of The Total Environment*, **905**, https://doi.org/10.1016/j.scitotenv.2023.167306, URL https://www.sciencedirect.com/science/article/pii/S0048969723059338.

NTSB, 2021: Preventing Turbulence-Related Injuries in Air Carrier Operations Conducted Under Title 14 Code of Federal Regulations Part 121. National Transportation Safety Board Tech. Report, NTSB, 115 pp.

Prandtl, L., 1928: Motion of Fluids With Very Little Viscosity. URL https://digital.library.unt.edu/ark:/67531/metadc65275/.

Proud, S. R., 2015: Analysis of aircraft flights near convective weather over Europe. *Weather*, **70 (10)**, 292–296, https://doi.org/10.1002/wea.2569, URL https://rmets.onlinelibrary.wiley.com/doi/10.1002/wea.2569.

Reynolds, O., 1883: III. An experimental investigation of the circumstances which determine whether the motion of water shall be direct or sinuous, and of the law of resistance in parallel channels. *Proceedings of the Royal Society of London*, **35 (224-226)**, 84–99, https://doi.org/10.1098/rspl.1883.0018, URL https://doi.org/10.1098/rspl.1883.0018.

Roach, W. T., 1970: On the influence of synoptic development on the production of high level turbulence. *Quarterly Journal of the Royal Meteorological Society*, **96 (409)**, https://doi.org/10.1002/qj.49709640906, URL https://onlinelibrary.wiley.com/doi/abs/10.1002/qj.49709640906.

Sharman, R., 2016: Nature of Aviation Turbulence. *Aviation Turbulence: Processes, Detection, Prediction*, R. Sharman, and T. Lane, Eds., Springer International Publishing, Cham, 3–30, https://doi.org/10.1007/978-3-319-23630-8_1, URL https://doi.org/10.1007/978-3-319-23630-8_1.

Sharman, R., C. Tebaldi, G. Wiener, and J. Wolff, 2006: An Integrated Approach to Mid- and Upper-Level Turbulence Forecasting. *Weather and Forecasting*, **21 (3)**, 268–287, https://doi.org/10.1175/WAF924.1, URL https://journals.ametsoc.org/view/journals/wefo/21/3/waf924_1.xml.

Sharman, R. D., L. B. Cornman, G. Meymaris, J. Pearson, and T. Farrar, 2014: Description and Derived Climatologies of Automated In Situ Eddy-Dissipation-Rate Reports of Atmospheric Turbulence. *Journal of Applied Meteorology and Climatology*, **53 (6)**, 1416–1432, https://doi.org/10.1175/JAMC-D-13-0329.1, URL https://journals.ametsoc.org/view/journals/apme/53/6/jamc-d-13-0329.1.xml.

Sharman, R. D., and J. M. Pearson, 2017: Prediction of Energy Dissipation Rates

for Aviation Turbulence. Part I: Forecasting Nonconvective Turbulence. *Journal of Applied Meteorology and Climatology*, **56 (2)**, 317–337, https://doi.org/10.1175/JAMC-D-16-0205.1, URL https://journals.ametsoc.org/view/journals/apme/56/2/jamc-d-16-0205.1.xml.

Sharman, R. D., and S. B. Trier, 2019: Influences of Gravity Waves on Convectively Induced Turbulence (CIT): A Review. *Pure and Applied Geophysics*, **176 (5)**, 1923–1958, https://doi.org/10.1007/s00024-018-1849-2, URL https://doi.org/10.1007/s00024-018-1849-2.

Steiner, M., R. A. Houze, and S. E. Yuter, 1995: Climatological Characterization of Three-Dimensional Storm Structure from Operational Radar and Rain Gauge Data. *Journal of Applied Meteorology and Climatology*, **34 (9)**, 1978–2007, URL https://journals.ametsoc.org/view/journals/apme/34/9/1520-0450_1995_034_1978_ccotds_2_0_co_2.xml.

Stokes, G., 1865: On the Effect of the Internal Friction of Fluids on the Motion of Pendulums. *Mathematical and Physical Papers*, G. Stokes, Ed., Cambridge Library Collection - Mathematics, Vol. 3, Cambridge University Press, Cambridge, 1–10, https://doi.org/10.1017/CBO9780511702266.002, URL https://www.cambridge.org/core/books/mathematical-and-physical-papers/on-the-effect-of-the-internal-friction-of-fluids-on-the-motion-of-pendulums/11038EBC1E2D897D9E5B1297C9AE5D99.

Storer, L. N., P. D. Williams, and M. M. Joshi, 2017: Global Response of Clear-Air Turbulence to Climate Change. *Geophysical Research Letters*, **44 (19)**, https://doi.org/10.1002/2017GL074618, URL https://onlinelibrary.wiley.com/doi/abs/10.1002/2017GL074618.

Strauss, L., S. Serafin, S. Haimov, and V. Grubišić, 2015: Turbulence in breaking mountain waves and atmospheric rotors estimated from airborne in situ and Doppler radar measurements. *Quarterly Journal of the Royal Meteorological Society*, **141 (693)**, 3207–3225, https://doi.org/https://doi.org/10.1002/qj.2604, URL https://rmets.onlinelibrary.wiley.com/doi/10.1002/qj.2604.

Tinney, E. N., C. R. Homeyer, L. Elizalde, D. F. Hurst, A. M. Thompson, R. M. Stauffer, H. Vömel, and H. B. Selkirk, 2022: A Modern Approach to a Stability-Based Definition of the Tropopause. *Monthly Weather Review*, **150 (12)**, 3151–3174, https://doi.org/10.1175/MWR-D-22-0174.1, URL https://journals.ametsoc.org/view/journals/mwre/150/12/MWR-D-22-0174.1.xml.

Trier, S. B., and R. D. Sharman, 2009: Convection-Permitting Simulations of the Environment Supporting Widespread Turbulence within the Upper-Level Outflow

of a Mesoscale Convective System. *Monthly Weather Review*, **137 (6)**, 1972–1990, https://doi.org/10.1175/2008MWR2770.1, URL https://journals.ametsoc.org/view/journals/mwre/137/6/2008mwr2770.1.xml.

Trier, S. B., and R. D. Sharman, 2018: Trapped Gravity Waves and Their Association with Turbulence in a Large Thunderstorm Anvil during PECAN. *Monthly Weather Review*, **146 (9)**, 3031–3052, https://doi.org/10.1175/MWR-D-18-0152.1, URL https://journals.ametsoc.org/view/journals/mwre/146/9/mwr-d-18-0152.1.xml.

Trier, S. B., R. D. Sharman, and T. P. Lane, 2012: Influences of Moist Convection on a Cold-Season Outbreak of Clear-Air Turbulence (CAT). *Monthly Weather Review*, **140 (8)**, 2477–2496, https://doi.org/10.1175/MWR-D-11-00353.1, URL https://journals.ametsoc.org/view/journals/mwre/140/8/mwr-d-11-00353.1.xml.

Trier, S. B., R. D. Sharman, D. Muñoz-Esparza, and T. L. Keller, 2022: Effects of Distant Organized Convection on Forecasts of Widespread Clear-Air Turbulence. *Monthly Weather Review*, **150 (10)**, 2593–2615, https://doi.org/10.1175/MWR-D-22-0077.1, URL https://journals.ametsoc.org/view/journals/mwre/150/10/MWR-D-22-0077.1.xml.

Uccellini, L. W., and S. E. Koch, 1987: The Synoptic Setting and Possible Energy Sources for Mesoscale Wave Disturbances. *Monthly Weather Review*, 721–729, URL https://journals.ametsoc.org/view/journals/mwre/115/3/1520-0493_1987_115_0721_tssape_2_0_co_2.xml.

Williams, P. D., and M. M. Joshi, 2013: Intensification of winter transatlantic aviation turbulence in response to climate change. *Nature Climate Change*, **3 (7)**, 644–648, https://doi.org/10.1038/nclimate1866, URL https://www.nature.com/articles/nclimate1866.

Wingrove, R. C., and R. E. Bach, 1994: Severe turbulence and maneuvering from airline flight records. *Journal of Aircraft*, **31 (4)**, 753–760, https://doi.org/10.2514/3.46557, URL https://arc.aiaa.org/doi/10.2514/3.46557.

Wolff, J. K., and R. D. Sharman, 2008: Climatology of Upper-Level Turbulence over the Contiguous United States. *Journal of Applied Meteorology and Climatology*, **47 (8)**, 2198–2214, https://doi.org/10.1175/2008JAMC1799.1, URL https://journals.ametsoc.org/view/journals/apme/47/8/2008jamc1799.1.xml.